APPL endosomes are not obligatory endocytic intermediates but act as stable cargo-sorting compartments

Inna Kalaidzidis,[1]* Marta Miaczynska,[1,2]* Marta Brewińska-Olchowik,[2,3]* Anna Hupalowska,[2] Charles Ferguson,[4] Robert G. Parton,[4] Yannis Kalaidzidis,[1,5] and Marino Zerial[1]

[1]Max Planck Institute of Molecular Cell Biology and Genetics, 01307 Dresden, Germany
[2]International Institute of Molecular and Cell Biology, 02-109 Warsaw, Poland
[3]Nencki Institute of Experimental Biology, 02-093 Warsaw, Poland
[4]Institute for Molecular Bioscience and Centre for Microscopy and Microanalysis, University of Queensland St. Lucia, Brisbane, Australia 4072
[5]Faculty of Bioengineering and Bioinformatics, Lomonosov Moscow State University, 119991 Moscow, Russia

Endocytosis allows cargo to enter a series of specialized endosomal compartments, beginning with early endosomes harboring Rab5 and its effector EEA1. There are, however, additional structures labeled by the Rab5 effector APPL1 whose role in endocytic transport remains unclear. It has been proposed that APPL1 vesicles are transport intermediates that convert into EEA1 endosomes. Here, we tested this model by analyzing the ultrastructural morphology, kinetics of cargo transport, and stability of the APPL1 compartment over time. We found that APPL1 resides on a tubulo-vesicular compartment that is capable of sorting cargo for recycling or degradation and that displays long lifetimes, all features typical of early endosomes. Fitting mathematical models to experimental data rules out maturation of APPL1 vesicles into EEA1 endosomes as a primary mechanism for cargo transport. Our data suggest instead that APPL1 endosomes represent a distinct population of Rab5-positive sorting endosomes, thus providing important insights into the compartmental organization of the early endocytic pathway.

Introduction

Endocytosis enables the internalization of extracellular molecules into a series of intracellular membrane compartments. In the simplest view of the endocytic pathway, cargo endocytosed from the plasma membrane is transported to early endosomes, where it is sorted for recycling (e.g., transferrin [Tf]) or degradation (e.g., EGF). However, the discovery that cargo can be internalized by both clathrin-dependent (CDE) and clathrin-independent (CIE) endocytosis (CDE), and delivered to various endocytic compartments (Conner and Schmid, 2003; Mayor and Pagano, 2007; Doherty and McMahon, 2009) revealed a much greater complexity of the endocytic pathway than initially envisaged. Besides different endocytic vesicles, there is also evidence for different populations of early endosomes on the basis of molecular markers and cargo sorting (Miaczynska et al., 2004; Lakadamyali et al., 2006). Early endosomes are characterized by the presence of the small GTPase Rab5 (Chavrier

et al., 1990; Zerial and McBride, 2001; Stenmark, 2009; Pfeffer, 2013), phosphatidylinositol 3-phosphate (PI(3)P), and Rab5 effectors, such as EEA1 (Simonsen et al., 1998; Christoforidis et al., 1999). From these early endosomes, cargo can be recycled to the surface or targeted for degradation via conversion of Rab5 early endosomes into Rab7 late endosomes (Rink et al., 2005; Poteryaev et al., 2010; Foret et al., 2012). Consistent with the view that late endosomes are dependent on early endosomes, loss of Rab5 impairs biogenesis of the entire endo-lysosomal pathway (Zeigerer et al., 2012). Thus, Rab5-positive endosomes act as a central sorting hub.
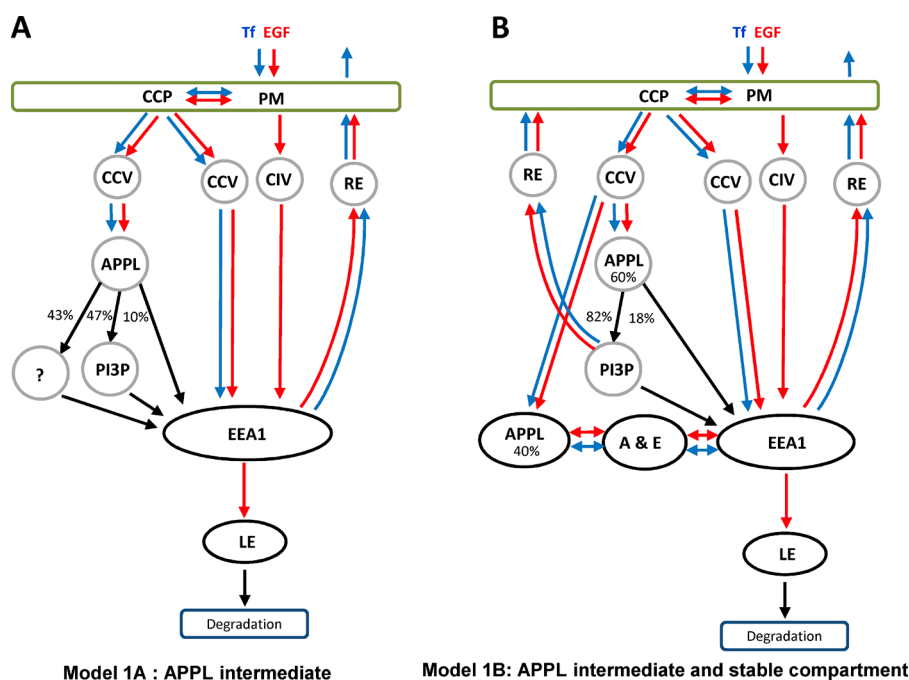
Studies have shown that some Rab5-positive early endosomes contain the effectors APPL1 and APPL2 (referred to here more generally as APPL1 endosomes), which show only limited colocalization with EEA1 and other organelle markers (Miaczynska et al., 2004). APPL proteins interact with specific sets of receptors (Mao et al., 2006) and signaling molecules (Mitsuuchi et al., 1999), and there is increasing evidence that they modulate signaling in various pathways, such as nerve growth factor (Lin et al., 2006; Varsano et al.,

---

*I. Kalaidzidis, M. Miaczynska, and M. Brewińska-Olchowik contributed equally to this paper.

Correspondence to Marino Zerial: zerial@MPI-CBG.de

Abbreviations used in this paper: BAC, bacterial artificial chromosome; CCP, clathrin-coated pit; CCV, clathrin-coated vesicle; CDE, clathrin-dependent endocytosis; CDI, clarithin-independent endocytosis; CHC, clathrin heavy chain; esiRNA, endoribonuclease-prepared small interfering RNA; ODE, ordinary differential equation; PI(3)P, phosphatidylinositol 3-phosphate; PM, plasma membrane; Tf, transferrin.

THE JOURNAL OF CELL BIOLOGY

A Model 1A : APPL intermediate

B Model 1B: APPL intermediate and stable compartment

Figure 1. **Models of cargo trafficking through APPL and EEA1 compartments.** (A) In model 1, the APPL compartment serves as an intermediate en route to EEA1-positive endosomes. Cargo first binds to receptors on the PM and is internalized via CDE or CIE. The CDE includes formation of CCPs and internalization CCVs. Some CCVs acquire APPL1 or fuse with APPL1 membranes. Other CCVs and CIV directly fuse with EEA1 endosomes. APPL1 vesicles directly (10% through an APPL1+EEA1 double-positive endocytic intermediate [A & E]) or indirectly (47%+43%) convert into EEA1 endosomes. Cargo can be recycled to the surface via recycling endosomes (RE) or transported to late endosomes (LE) and lysosomes for degradation. Blue and red arrows demark transport of Tf and EGF, respectively. Black arrows, steps that must be common for both cargos. (B) In model 2, APPL1 endosomes that were not accounted in the literature (43%) constitute a stable endocytic compartment. These endosomes sort cargo for recycling and bi-directionally exchange of cargo with EEA1 endosomes through APPL1+EEA1 double-positive endosomes. Transition to late endocytic compartment occurs through EEA1 by conversion mechanism.

2006), lysophosphatidic acid (Varsano et al., 2012), adiponectin (Mao et al., 2006; Deepa and Dong, 2009; Xin et al., 2011), Akt (Schenck et al., 2008; Wang et al., 2012), insulin (Cheng et al., 2012), Wnt (Rashid et al., 2009), and nuclear factor κB (Hupalowska et al., 2012). These studies led to the hypothesis that APPL-positive structures constitute a separate endosomal population, processing a subset of cargo with different transport kinetics and functional specificity.

Live-cell imaging studies have supported an alternative model (see Fig. 1 A) in which APPL vesicles/endosomes behave as transport intermediates in the generation of EEA1-positive early endosomes (Erdmann et al., 2007; Zoncu et al., 2009) via a process that resembles Rab5-to-Rab7 conversion (Rink et al., 2005). This model is based on the observations that endocytic clathrin-coated vesicles (CCVs) sequentially acquire OCRL and APPL1, and generate PI(3)P, resulting in the loss of APPL1 and acquisition of EEA1. Although the APPL1/EEA1 conversion model is widely accepted in the field (Di Fiore and von Zastrow, 2014), only ∼10% of APPL1 endosomes have been proposed to directly convert into EEA1 endosomes (Erdmann et al., 2007; Zoncu et al., 2009). A further 47% convert via a PI(3)P- and WDFY2-positive intermediate (Zoncu et al., 2009). In both cases, the conversion mechanism implies that the whole content of a vesicle/endosome must be retained in the following compartment without cargo selectivity. Additionally, the fate of the remaining 43% of APPL1 endosomes remains unclear. One possibility is that these endosomes also act as transient intermediates and subsequently convert into EEA1 endosomes (Fig. 1 A). Alternatively, they could be long-lived compartments that sort cargo and dynamically exchange it with EEA1 endosomes (Fig. 1 B). The two models predict very different kinetics of cargo transport through APPL1 and EEA1 endosomes. Furthermore, recent studies have shown that cargo transport to EEA1 endosomes does not necessarily traverse an APPL1 vesicular intermediate (Danson et al., 2013; Flores-Rodriguez et al., 2015). Altogether, these observations raise several questions. To what extent are APPL structures distinct from EEA1 endosomes?

Do they have a simple vesicular morphology or are they pleomorphic similar to endosomes? Do different types of cargo flow through APPL- and EEA1-compartments with similar kinetics, and does APPL-EEA1 conversion best describe such kinetics? Are APPL structures capable of cargo sorting and stable throughout cargo transport? If so, can APPL and EEA1 endosomes exchange cargo dynamically?

Here, we used a combination of electron microscopy, live-cell imaging, and kinetic analysis in both wild-type and perturbed cells to analyze the morphology, dynamics, and kinetics of cargo transport of APPL1- and EEA1-positive compartments. Subsequently, we applied a system-identification approach to define the simplest model that can describe the experimental data. Our data indicate that conversion of APPL1 vesicles into EEA1 endosomes is not a primary mechanism for cargo transport and that the APPL1 compartment instead functions as an authentic sorting endosome. On this basis, we propose a novel model for the organization of the early endocytic pathway.

Results

APPL1 protein labels a subpopulation of tubulo-vesicular early endosomes

To characterize the APPL1-positive vesicles, we used anti-APPL1 antibodies to detect the endogenous protein in HeLa cells. The staining confirmed the pattern of APPL1 on small punctate structures, several of which reside close or adjacent to the plasma membrane (Miaczynska et al., 2004). These were distinct from clathrin-coated pits (CCPs) and CCVs (Fig. S1 A), in agreement with previous findings that APPL1 does not reside on CCPs (Erdmann et al., 2007). APPL1 staining also had no significant overlap with various markers of the biosynthetic or late endocytic pathway (Fig. S1 A).

We next used immunoelectron microscopy to analyze the ultrastructure of APPL1-labeled vesicles. Although we have previously used this method on frozen sections, labeling of the
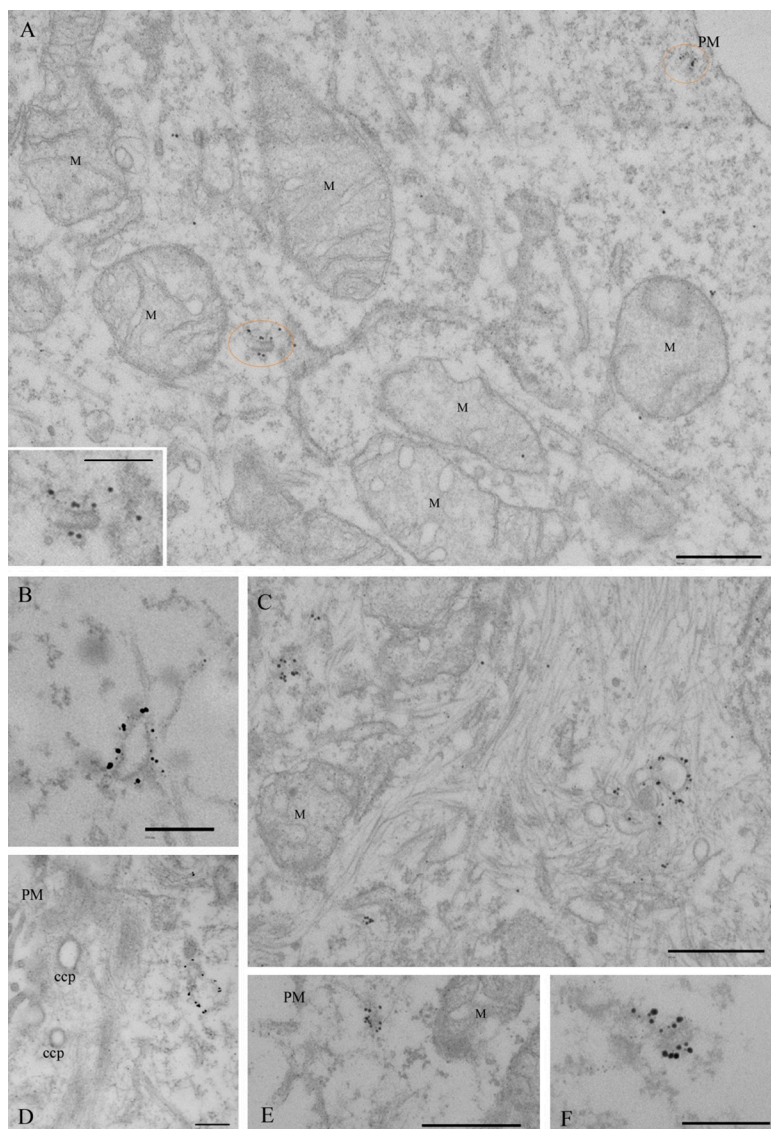
Figure 2. **Immunoelectron microscopic localization of APPL1.** HeLa cells were labeled with antibodies to APPL1, followed by a Nanogold-labeled conjugate. Gold particles were visualized by silver enhancement. (A) A low-magnification view with two APPL-positive structures circled in orange, one of which is shown at higher magnification in the inset. (B–F) A gallery of representative structures. Dense labeling is associated with small tubular profiles close to the PM or deeper inside the cell as well as with larger heterogeneous structures. Note that labeling of the PM or CCPs is very low. M, mitochondria. Bars: (A, C, and E) 500 nm; (A [inset], B, D, and F) 200 nm.

endogenous protein was invariably low with all available APPL1 antibodies, making a detailed characterization of the labeled compartments difficult. We therefore used a preembedding approach to localize APPL1 using digitonin for permeabilization, and labeling with 1 nm Nanogold (Nanoprobes), followed by silver enhancement and plastic embedding.

Specific labeling was observed on distinct morphologic membrane-bound structures. Dense labeling was associated with tubulo-vesicular structures with a mean diameter of 49 ± 0.2 nm (*n* = 15) and of variable length (up to 260 nm in thin sections; Fig. 2). Consistent with the light-microscopic observations, these densely labeled tubules were frequently observed very close to the plasma membrane (Fig. 2, A and E), but the plasma membrane itself showed very low labeling. Significant labeling was also observed on larger vacuolar structures (Fig. 2, B–D), which showed variable morphology, with diameters up to 360 nm. Labeling on other structures, including CCPs/CCVs (Fig. 2 D), was generally low compared with the putative endosomal elements.

Together, our results suggest that most APPL1-labeled structures are in the cell periphery and have a complex tubulo-vesicular morphology characteristic of early endosomes.

Inhibition of clathrin-dependent endocytosis does not deplete APPL1 endosomes

The model of biogenesis of APPL1 endosomes based on CCV maturation was supported by the finding that clathrin depletion caused a marked reduction in the number of APPL1 endosomes (∼60%; Zoncu et al., 2009). To corroborate these findings, we used two means to block CDE. First, we silenced clathrin heavy chain (CHC) using a previously validated siRNA (Motley et al., 2003; Fig. 3 A). The loss of clathrin function was demonstrated by a strong inhibition (90%) of Tf internalization, as assessed biochemically (Fig. 3 B) and by quantitative microscopy analysis (Fig.3, C–E). As a consequence, the colocalization of internalized Tf with both APPL1 and EEA1 was severely reduced (Fig. 3 C). Surprisingly, the number of APPL1 endosomes remained unchanged (Fig. 3, D–F). Silencing of CHC using the exact pair of siRNAs used by Zoncu et al. (2009) gave similar results despite the inhibition of Tf and EGF uptake (not depicted).

As an independent approach, we inhibited clathrin-mediated internalization using the dynamin inhibitor Dynasore (Macia et al., 2006). Dynasore markedly reduced Tf internalization, as judged by the 80% reduction of total vesicular
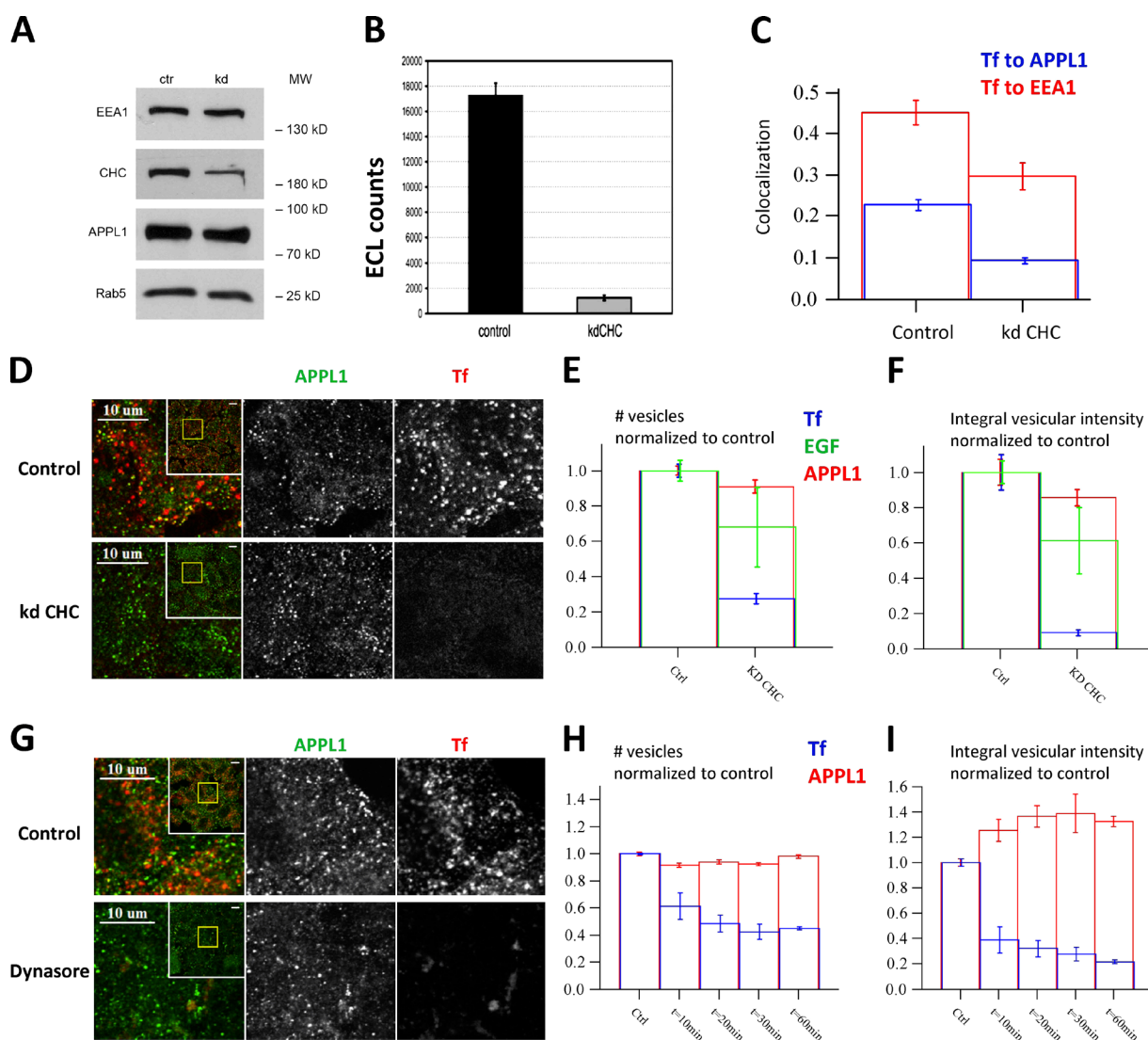
Figure 3. **Cargo internalization into APPL endosomes is clathrin dependent but their biogenesis is not.** (A) Silencing of CHC by RNAi in HeLa cells assessed by Western blot in comparison to EEA1, APPL1, and Rab5 as controls. (B) Internalization of biotinylated Tf (b-Tf) (after 30 min of continuous uptake) is inhibited upon CHC knockdown. The amounts of b-Tf in cell lysates were quantified by electrochemiluminescence. (C) Knockdown of CHC decreased colocalization of Tf to EEA1 (red) and APPL1 (blue). Colocalization was quantified after 3.5-min chase after 0.5-min internalization pulse of Tf. (D–F) Knockdown of clathrin inhibits Tf uptake but does not affect the number of APPL1-positive vesicles. Example images of endogenous APPL1 and fluorescent Tf at 3.5-min chase after the 30-s internalization pulse in control and clathrin-depleted cells (D). Inset presents full image, yellow rectangle depicts zoomed part. The numbers of vesicles marked by APPL1 (red), Tf (blue) or EGF (green) (E) and their integral intensities (F) are plotted (quantifications based on 80 images and ~320,000 APPL1 endosomes). (G–I) Dynasore treatment (from 10 to 60 min) does not affect the number of APPL1-positive vesicles but progressively suppresses Tf uptake (10 min of Tf internalization). (G) Example images of HeLa cells treated with Dynasore (80 µM) for 60 min. The numbers of vesicles marked by APPL1 (red) and Tf (blue) (H) and their integral intensities (I) in cells pretreated with Dynasore for the indicated times are plotted (quantifications based on 10 images, ~110 cells, and ~45,000 APPL1 endosomes). Bars: (D and G, inset) 10 µm.

fluorescence (Fig. 3, G–I). Again, the number of APPL1 endosomes was unaffected under these conditions, whereas the total vesicular fluorescence of APPL1 was even slightly increased. These results argue that the stability of APPL1 endosomes does not depend on the flow of incoming CCVs.

Stability of APPL1 endosomes
The findings that APPL1-positive structures have a complex morphology and persist when clathrin-mediated endocytosis is inhibited suggest that at least a fraction may be a stable endosomal compartment. We tested this prediction by live-cell imaging of HeLa cells transiently transfected with APPL1 tagged with EGFP at the N-terminus (EGFP-APPL1; see Materials

and methods). We first verified that EGFP-APPL1 expression caused no significant alterations on the endocytic system (e.g., number of endosomes; Fig. S2, A and B) and transport of Tf and EGF (Fig. S2, F–H). To measure the lifetime of EGFP-APPL1 endosomes, we recorded their dynamics by fast imaging using a spinning disc microscope, followed by tracking of individual endosomes using Motiontracking software (Rink et al., 2005). In parallel, we performed the same type of analysis on HeLa cells stably transfected with a bacterial artificial chromosome (BAC) transgene expressing EGFP-Rab5c under its endogenous promoter (HeLa BAC-EGFP-Rab5c; Foret et al., 2012). By tracking EGFP-APPL1 and EGFP-Rab5c endosomes, we found that the distribution of their lifetimes was
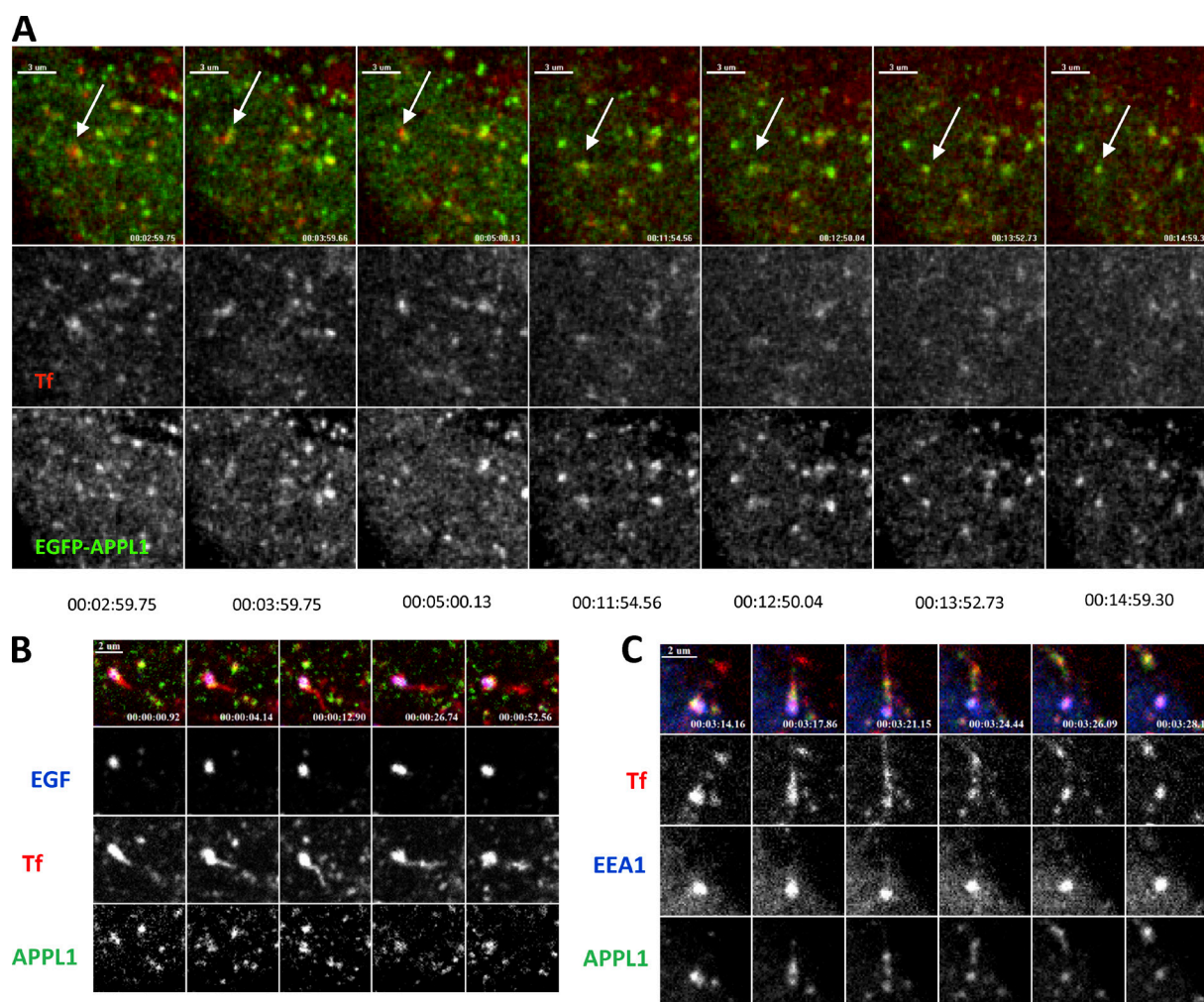
Figure 4. **APPL endosomes are stable structures.** (A) Gallery of images showing a long-lived APPL endosome (arrow) containing internalized Tf, tracked for 12 min in HeLa cells expressing EGFP-APPL1 (see Video 1). (B) APPL1 (green) endosome with EGF (blue) and Tf (red) sorts Tf from EGF. Tf-positive tubule growing over time and pinched-off from APPL1 endosome (see Video 3). (C) Double EEA1 (blue) + APPL1 (green) endosome produces Tf- (red) and APPL1-positive, EEA1-negative tubule (see Video 4). Later this tubule was separated from the main endosome body.

very similar (Fig. S2 I). Thus, EGFP-APPL1 endosomes are indistinguishable from the bulk of EGFP-Rab5c endosomes in terms of temporal stability.

To visualize the dynamic behavior of APPL1 endosomes with respect to internalized cargo, we recorded two-channel movies of cells expressing EGFP-APPL1 and labeled by internalized fluorescent Tf. Individual EGFP-APPL1–labeled endosomes containing Tf could be tracked for periods exceeding 10 min (Fig. 4 A and Video 1), indicating that a substantial fraction of APPL1 endosomes are long-lived.

Dynamics and sorting activity of APPL1 endosomes

We previously reported that a significant fraction (∼11%) of structures are positive for both APPL1 and EEA1 using a pixel-based colocalization approach (Miaczynska et al., 2004). Because we further improved our automated image analysis platform (http://motiontracking.mpi-cbg.de; Rink et al., 2005; Collinet et al., 2010) using an object-based quantification method (Kalaidzidis et al., 2015), we remeasured the overlap between APPL1 and EEA1 endosomes. The advantage of measuring colocalization between objects rather than individual pixels is that it allows for the compensation of chromatic aberrations and irreproducible per-frame misalignment of channels that significantly influence the colocalization analysis of small objects. We measured a colocalization value of 29.4% ± 8.5% (mean ± SD; ∼2,200 cells/experiment, four experiments) as the fraction of APPL1 associated with EEA1-positive membranes relative to the total amount of vesicular APPL1 (Fig. S1 B). Requantification of the original images in Miaczynska et al. (2004) yielded similar values. Because a substantial fraction of APPL1 colocalizes with EEA1, we explored the dynamics of the two proteins on the double-positive compartment. We expressed various GFP-tagged EEA1 constructs and quantified their intracellular distribution. Unfortunately, most tagged EEA1 constructs were mislocalized (Fig. S2 C). However, one construct, the tagRFP-T-EEA1 of Navaroli et al. (2012) showed the expected distribution (Fig. S2, D and E) and did not alter Tf and EGF trafficking (Fig. S2, F–H). Therefore, we used the tagRFP-T-EEA1 construct for further live cell imaging studies.

We recorded the dynamics of APPL1 endosomes with respect to EEA1 endosomes and cargo trafficking (Tf and EGF). To begin with, we found that EGFP-APPL1 was

highly dynamic and displayed fast motility accompanied by fusion and fission events between cargo-loaded endosomes (Video 1). To monitor this behavior, we captured images in a single z-plane with three channels at the highest achievable frame rate to allow imaging without significant phototoxicity (2.5 frame/s). We recorded combinations of (a) EGFP-APPL1, Tf, and EGF; (b) EGFP-APPL1, tagRFP-T-EEA1, and Tf; and (c) EGFP-APPL1, tagRFP-T-EEA1, and EGF. Because the high motility of APPL1- and EEA1-positive endosomes and the crowded cytoplasm made automated analysis of fusion/fission events a challenging task, we were obliged to inspect and analyze the movies manually. Altogether, we analyzed 34 movies with two to three cells per movie.

We found that the most frequent events were fusion and fission of small APPL1-positive endosomes (Video 2). The frequency of these events was too high for accurate manual counting, and therefore we did not include them in the summary statistics (Fig. 5 E). Second, we found that APPL1-positive endosomes were capable of separating Tf from EGF by emanating Tf-positive, APPL1-negative, and EGF-negative tubules (Fig. 4 B and Video 3), demonstrating that they are bona fide sorting endosomes. Third, we uncovered multiple modes of interaction between APPL1-positive, EEA1-positive, and EEA1+APPL1 double-positive endosomes. Representative examples of the observed events and their frequency are shown in Fig. 5 (A–E). Surprisingly, we could observe fission of APPL1 and Tf structures from EEA1+APPL1–positive endosomes (Fig. 4 C and Video 4)—that is, traffic of cargo in the opposite direction of that predicted by a model based on APPL1-positive structures as transient intermediates (Fig. 1 A). The main mode (~65%) of traffic from APPL1 to EEA1 endosomes was the fusion of APPL1-positive endosomes with EEA1- or with APPL1+EEA1–positive endosomes (Fig. 5, A, B, and E; and Videos 5 and 6). The second most frequent event (~15%) was the fission of APPL1 membranes from APPL1+EEA1 endosomes. The direct fast conversion of APPL1 endosomes into EEA1 endosomes (Erdmann et al., 2007; Zoncu et al., 2009) was an extremely rare event (only 2 events out of 234). On the other hand, we repeatedly detected the loss of APPL1 from APPL1+EEA1–positive endosomes (Fig. 5, C and E; and Video 7) and the acquisition of EEA1 by APPL1 endosomes. However, these were not sequential steps of APPL1 to EEA1 conversion. APPL1+EEA1 endosomes were long-living entities, displayed multiple fusion/fission events and interactions with other endosomes, and existed from the beginning of the corresponding time-lapse movies. Surprisingly, even more frequently we detected conversion of APPL1+EEA1 endosomes into APPL1-positive and EEA1-negative endosomes (Fig. 5, D and E; and Video 8). The frequency of events therefore suggests that most interactions between APPL1- and EEA1-positive endosomes occur through preexisting APPL1+EEA1 endosomes. These endosomes have a pleomorphic morphology, dynamically evolve over time and, on average, are larger than APPL1-positive endosomes (Figs. S2 J and S1 F). The behavior of the APPL1+EEA1 endosomes rules out the possibility that this compartment can be the conversion intermediate described by Zoncu et al. (2009), as this exhibited a lifetime of 20 s/1 min. We conclude that the APPL1+EEA1 double-positive endosomes constitute a compartment that serves as an interaction hub between the two distinct populations of APPL1- and EEA1-positive early endosomes.

## Quantitative analysis of cargo transport via APPL1- and EEA1-positive compartments

Our data so far suggest that the APPL1 compartment is an endosome capable of cargo sorting. Because our live-cell imaging set-up can measure only three markers simultaneously and lack the necessary throughput to generate a detailed quantitative model of cargo transport through APPL1 and EEA1 endosomes, we took a system-identification approach to define the simplest model that would explain the experimental data. Briefly, we performed a detailed kinetic analysis of cargo transport through both compartments. Then, we formulated mathematical models corresponding to the schemes presented in Fig. 1 (A and B) and fit their parameters to the experimental data. Finally, we made a probabilistic assessment of how well the models explain the experimental data.

We established a pulse-chase protocol for the simultaneous uptake of fluorescently labeled Tf and EGF. HeLa cells were given a 30-s pulse of Tf and EGF, chased for various times (0–30 min, 14 time points) and immunostained for endogenous APPL1 and EEA1 (Fig. 6 A). A 10-fold excess of nonfluorescent Tf was added to the chase medium to prevent reinternalization of labeled tracers, thus limiting the analysis to one cycle of Tf entry and exit. This assay provided us with spatial and temporal resolution in order to (a) follow a very short, single wave of internalized cargo in cells expressing endogenous levels of APPL1 and EEA1 and (b) obtain statistically significant, quantitative data. In a standard experiment, at least 10 four-channel confocal images per time point with 15–20 cells per image were analyzed using Motiontracking. Altogether, ~140,000 Tf-positive and 120,000 EGF-positive endosomes were analyzed per time point (four experiments). This allowed us to acquire large-scale, high-resolution kinetic data regarding cargo transit in the cell.

We validated our quantitative image analysis approach using an independent biochemical method with electrochemiluminescence (Horiuchi et al., 1997; Ohya et al., 2009) to assess the intracellular content of biotinylated Tf internalized under the same conditions of fluorescent cargo (30-s pulse, 0- to 30-min chase). The two methods produced very similar kinetics of intracellular accumulation of biotinylated or fluorescent Tf (Fig. S1, compare C with D). We further quantified the total amount of cargo inside the cells throughout the 30-min chase period after the internalization pulse (Fig. S1 C). Tf reached the maximal intracellular accumulation already within 5 min after uptake and was subsequently recycled. In contrast, EGF progressively accumulated in cells, reached the maximum after 10 min, and remained constant until 30 min (Fig. S1 C).

To determine the spatial and temporal progression of Tf and EGF through APPL1 and EEA1 endosomes, we calculated the amount of cargo colocalizing with either endocytic marker or none at every time point of the chase (Fig. 6, B and C). Both Tf and EGF were transported through endosomes containing APPL1, EEA1, or both, with substantially different kinetics and efficiency. The colocalization of EGF and Tf gradually increased over the first 10 min (e.g., reaching 60% at 12.5 min; Fig. 6 D). This means that EGF and Tf can enter via different vesicles or with different kinetics but meet in the same endosomes, thus ruling out that they are trafficked by different subpopulations of endosomes. Tf entered APPL1 endosomes rapidly and slightly faster than EEA1 endosomes (blue curve in Fig. 6 B; see inset), achieving maximal
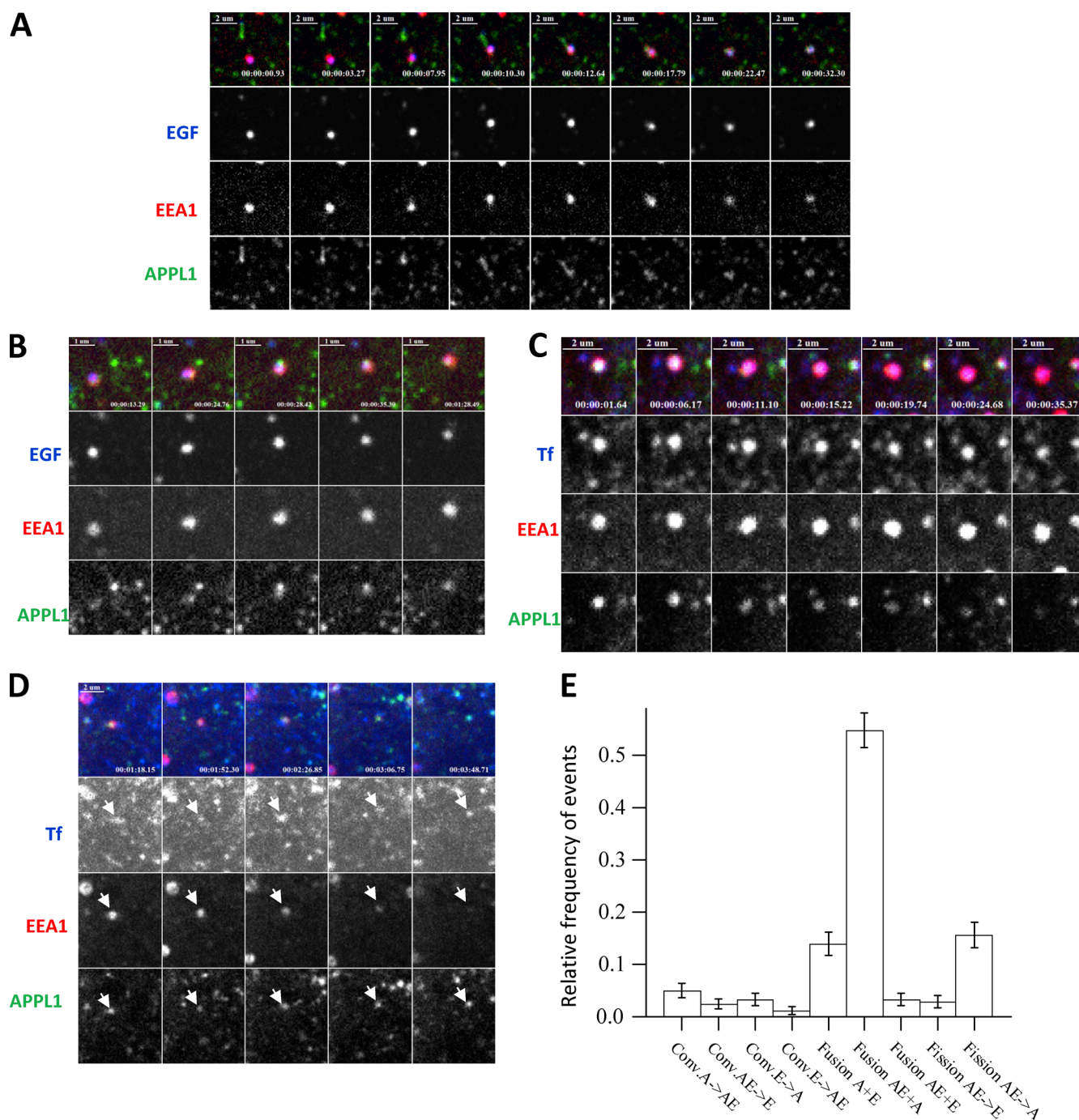
Figure 5. **APPL endosomes exhibit features of cargo sorting by live cell imaging.** (A) Sequential images showing an EEA1-positive APPL1-negative vesicle carrying EGF, which fuses with multiple preexisting APPL1 endosomes (see Video 5). (B) Sequential images depicting fusion of a double APPL1+EEA1–positive endosome with an APPL1-positive endosome (see Video 6). (C) Double APPL1+EEA1 endosome gradually loses APPL1 and converts to EEA1 endosome (see Video 7). (D) Double APPL1+EEA1–positive endosome gradually loses EEA1 and converts to APPL1 endosome (see Video 8). (E) Relative frequencies of individual events of interaction between APPL1- (A), EEA1- (E), and double APPL1+EEA1 (AE)–positive endosomes (error bars represent SEMs). Data were collected from 34 movies. Total number of events equals 234.

accumulation at 2 min after internalization. In contrast, EGF entered first EEA1 endosomes (red curve in Fig. 6 C) but accumulated slowly in APPL1 endosomes, peaking after 5 min of internalization (blue curve in Fig. 6 C). The maximal amounts of both Tf and EGF were lower in APPL1 than EEA1 endosomes. Strikingly, a substantial fraction of Tf and EGF was transported through APPL1+EEA1 compartments (green curves in Fig. 6, B and C). In general, it appeared that cargo

resided longer in APPL1+EEA1 endosomes. Furthermore, the kinetics of Tf and EGF exiting APPL1 endosomes were different (blue curves in Fig. 6, B and C). Despite ongoing recycling, APPL1, EEA1, and APPL1+EEA1 endosomes retained a fraction of Tf throughout the whole chase period (Fig. 6 B). In contrast, after a 15-min chase, APPL1 endosomes were devoid of EGF, which was present in EEA1- or APPL1+EEA1–positive structures (Fig. 6 C).
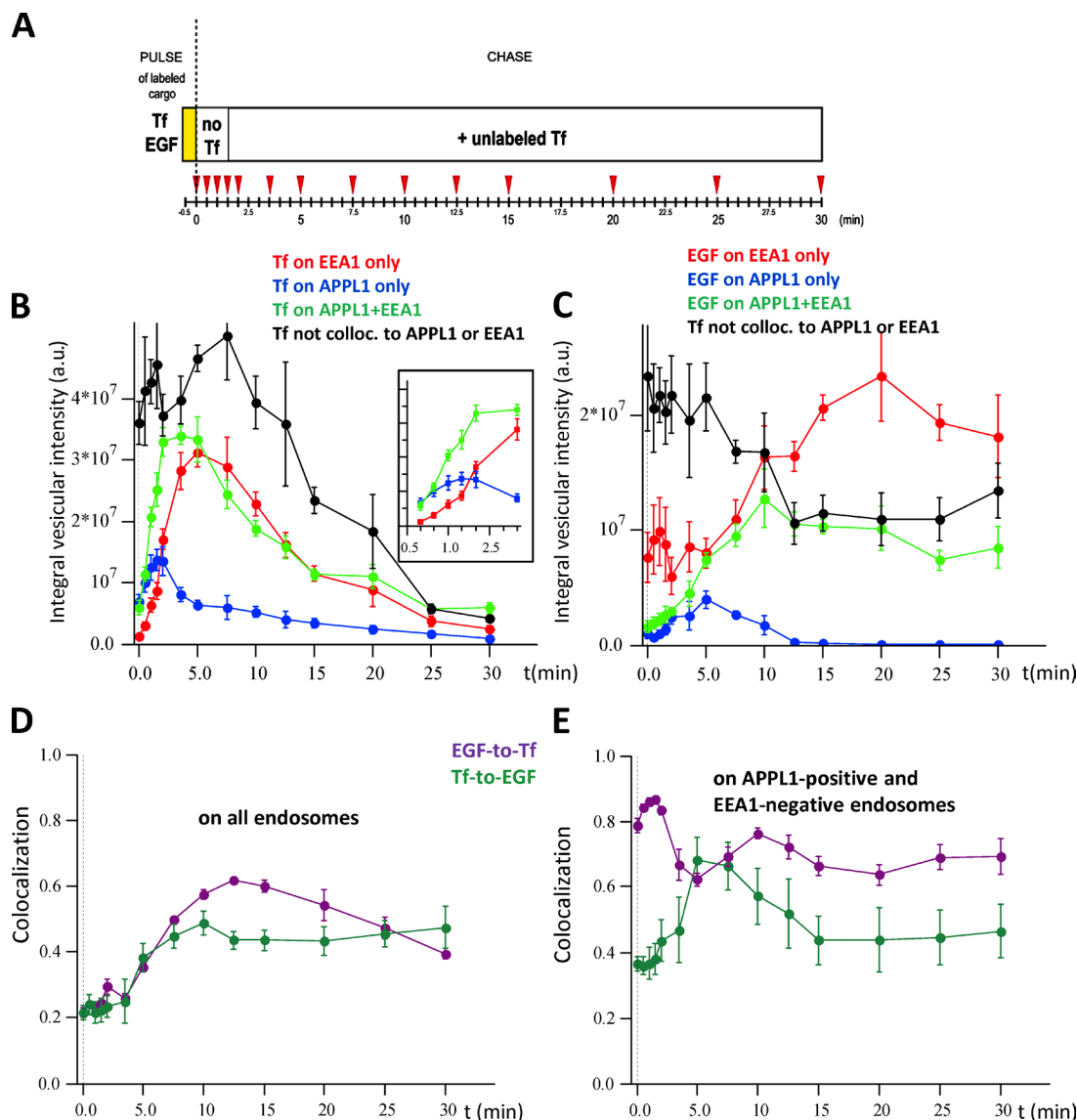
Figure 6. **Time course of cargo distribution in EEA1- and APPL1-positive structures.** Fluorescently labeled Tf and EGF were internalized for 30 s and chased for the indicated periods of time (A). All experimental data are the mean of four independent experiments. The intensity of Tf and EGF colocalized to EEA1 and APPL1 was corrected for apparent (random) colocalization (Kalaidzidis et al., 2015). (B and C) Kinetics of fluorescence intensity of Tf (B) or EGF (C) colocalized with EEA1-positive and APPL1-negative endosomes (red), APPL1-positive and EEA1-negative endosomes (blue), with double EEA1+APPL1–positive endosomes (green) and colocalized with none of them (black). The inset shows the part of the curve corresponding to the initial 3 min of the time course. (D) Time course of colocalization of EGF-with-Tf (magenta) and Tf-with-EGF (green) on all endosomes. (E) Time course of colocalization of EGF-with-Tf (magenta) and Tf-with-EGF (green) on APPL1-positive and EEA1-negative endosomes. This colocalization is defined as the ratio of the amount of EGF colocalized with Tf on APPL1 endosomes to the total amount of EGF on APPL endosomes. The same applies to Tf-with-EGF colocalization on APPL endosomes. Error bars represent SEMs.

Most APPL1 endosomes are not intermediates in cargo transport toward EEA1 endosomes

We next sought to determine whether our observations are compatible with models in which APPL-positive structures are exclusively intermediates (Fig. 1 A) or form both a stable compartment and intermediate structures (Fig. 1 B). We first formulated the models as sets of ordinary differential equations (ODEs) defining the different steps of cargo flux through a sequence of endocytic compartments (see Mathematical methods). The mathematical models allowed us to make quantitative predictions for the trafficking of different cargo tracers, such as Tf (recycling) and EGF (degradation), through APPL1 and

EEA1 endosomes (see Materials and methods). Second, we fit the parameters of the models to the kinetics of cargo transport determined experimentally. Third, we assessed the quality of the model predictions. For the kinetics data, we chose (a) the total amount of cargo; (b) colocalization of cargo to APPL1, EEA1, or APPL1+EEA1 endosomes; and (c) the fraction of cargo that does not colocalize with any of these markers. The choice of these kinetics was justified by the high accuracy of the measurements (168 experimental data points; see Materials and methods).

Model 1A (Fig. 1 A) has two fundamental implications: (a) A simple vesicular intermediate with competitive exchange of APPL1 for EEA1 (Zoncu et al., 2009) implies that the delivery

rate of EGF and Tf from APPL1 vesicles to EEA1 endosomes has to be the same for both types of cargo, and (b) there is no retrograde flux of cargo from EEA1 to APPL1 endosomes. It results in 26 ODEs with 29 independent rate constants (Mathematical methods, model 1A). Model 1B (Fig. 1 B) expands model 1A by introducing stable APPL1 endosomes (∼40% of total APPL1e endosomes), which bi-directionally exchange cargo with EEA1 endosomes via the APPL1+EEA1 compartment (Fig. 1 B). We described it by a set of 32 ODEs with 36 independent rate constants (Mathematical methods, model 1B).

We used a fitting algorithm based on a combination of descent gradient and simulated annealing (Griffiths et al., 1999) to fit the parameters of models to the experimental data (Zeigerer et al., 2012). The best fit of model 1A qualitatively described the total Tf flux fairly well but failed to explain the colocalization time course between Tf and APPL1 (Fig. S3 A). The colocalization of EGF to all endosomal classes fit better than that of Tf, but the prediction of total flux of EGF was poor (Fig. S3 B). The fit of model 1B (Fig. S3, C and D) gave much better results, with the predicted and experimental curves closely overlapping. However, there were significant differences in the first two minutes for total EGF uptake and colocalization of EGF to the APPL1+EEA1 double-positive compartment (Fig. S3 D, inset). To quantify the quality of the fit, we calculated the χ^2-square of the deviation of the model prediction from the experimental data and estimated the probability of the multiparametric models (Fig. 8, B and C), as described (Sivia and Carlile, 1992). The probability is a tradeoff of quality of the fit and complexity of the model. The higher probability of model 1B in comparison with model 1A ($\Delta\log(p) = 29$) suggests that the increase in model complexity is statistically justified by a decrease in χ^2. We then tested the null hypothesis that deviation of experimental data from model prediction is a result of random noise. The χ^2 test gave a p-value $< 10^{-<300}$ and p-value of 5.8×10^{-22} (model 1, A and B, respectively) rejecting the null hypothesis. We conclude that none of the models can satisfactorily explain the experimental data. This, together with the live cell imaging data, rules out that most APPL1 endosomes are intermediates of cargo transport to EEA1 endosomes.

A new model of cargo transport through different sub-populations of early endosomes

To formulate an alternative model, we introduced all possible interactions between APPL1, EEA1, and APPL1+EEA1 double-positive compartments, which are compatible with the live cell imaging data (Fig. 5 E). However, we failed to fit the data with reasonable accuracy (P > 0.05). The complex transport kinetics of EGF through EEA1 endosomes prompted us to consider the existence of two kinetically distinct subpopulations of EEA1 and APPL1+EEA1 endosomes. This resulted in a model that is described by 33 ODEs and 68 independent kinetic rates. The fit of the new model to the experimental data satisfied the null-hypothesis (P = 0.55). Some kinetic rates in the model were fitted to zero in all conditions and, therefore, removed. The remaining rates were tested one by one to remove steps from the model without significantly compromising the fit (P > 0.05) while increasing the probability of the model. The resulting model 2 (27 ODEs, 38 parameters) and corresponding fits are presented in Fig. 8 A and Fig. S5. The probability of model 2 is much higher than that of model 1, A and B ($\Delta\log(p)$ = 726 and $\Delta\log(p)$ = 357). The χ^2 test showed that deviation of

model 2 predictions from the experimental data were statistically insignificant (P > 0.1).

Fitting of rate constants in model 2 indicated that the exchange of Tf between APPL1 and APPL1+EEA1 compartment is bi-directional, in line with the live cell imaging observations (Fig. 5 E), but the exchange of EGF is unidirectional (the rate of back flux of EGF from APPL1+EEA1 to APPL1 was one of the parameters fitted to zero). Moreover, the rate constants for the forward flux of Tf from the APPL1 to the APPL1+EEA1 compartment were significantly different from those of EGF. Hence, the model implies that most cargo that enters APPL1 endosomes must be sorted to account for the different delivery rates and, therefore, cannot be transferred en bloc to EEA1 endosomes by conversion, consistent with the live cell imaging data (Fig. 5 E).

To verify the results of model fitting, we further analyzed the kinetics data to determine whether cargo sorting indeed occurs in APPL1 endosomes. Comparison of Tf and EGF colocalization with APPL1 revealed striking differences between their respective kinetics (Fig. 6, B and C): Whereas the value of colocalization of Tf to APPL1 remained greater than zero throughout the chase period (Fig. 6 B, blue curve), the colocalization of EGF to APPL1 decreased to zero after 15 min (Fig. 6 C, blue curve). Importantly, at 5-min chase, when EGF peaked in APPL1 endosomes, the colocalization of EGF with Tf and Tf with EGF on APPL1 endosomes was 63% ± 2% and 64% ± 5%, respectively (Fig. 6 D). This makes it unlikely that EGF and Tf pass through distinct subpopulations of APPL1 vesicles. These data again imply that most cargo passing through the APPL1 compartment is sorted, a notion that is incompatible with a vesicular transport intermediate.

Verification of the cargo transport model

To further validate model 2, we introduced various endocytic perturbations to reroute cargo between compartments. The rationale behind this approach is that the model must be able to explain new data only by adjusting existing parameters without the need to add new ones. For this, we repeated the detailed pulse-chase experiments under knockdown of CHC (95%), APPL1 (70%), and EEA1 (90%; Figs. 3 A and S4). Note that because APPL1 and EEA1 are also the markers of the endosomal compartments and, thus, their silencing may impair the detection of the endosomes, their depletion is not complete and the endosomes are still detectable despite the reduction in fluorescence intensity. Furthermore, we introduced additional parameters in the model to account for the loss of the dimmest endosomes (see Materials and methods). All perturbations caused a significant redistribution of cargo between the different early endosomes (Fig. 7, A–F). Such alterations are not a consequence of variation in surface receptor levels, as demonstrated by the unaltered total fluorescence intensity after 30 s of cargo pulse (Fig. S4 C).

Inhibition of CDE reduced the uptake of Tf by 90% (Fig. 3 F, blue bars). However, the uptake of EGF (applied at 1 µg/ml, 30 s) was reduced only by 40% (Fig. 3 F, green bars). This is consistent with previous findings that EGF uptake (in our case at high concentration) occurs equally via CDE and CIE (Motley et al., 2003; Sigismund et al., 2005, 2008). The knockdown of CHC blocked delivery of Tf to both APPL1- and EEA1-positive endosomes and redirected the residual endocytosed cargo to the APPL1+EEA1 compartment (Fig. 7 A). The fast phase of EGF delivery to EEA1 was unchanged but the slow phase was totally abrogated. Whereas
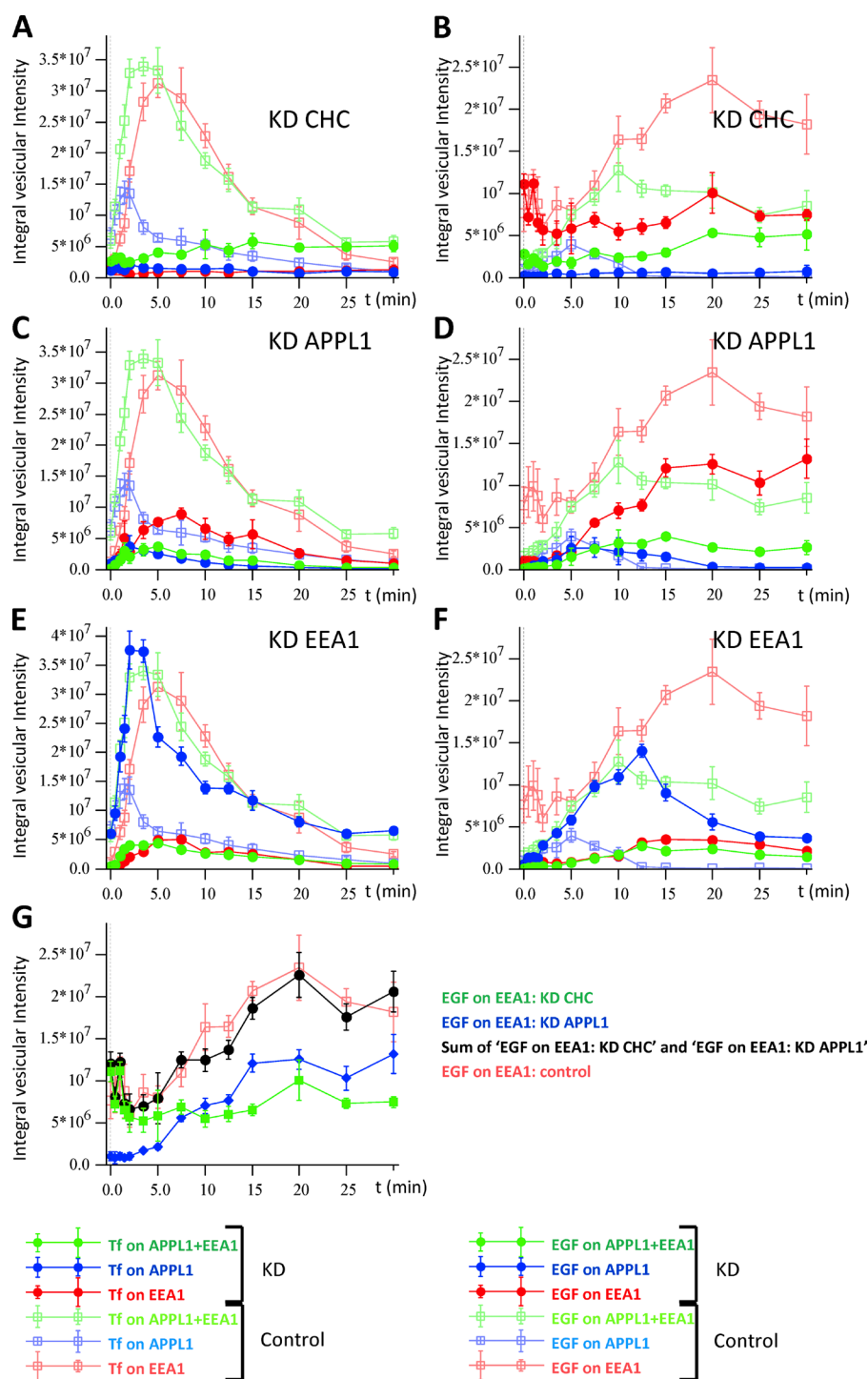
Figure 7. **Time course of Tf (A, C, and E) and EGF (B, D, and F) distribution in EEA1- and APPL1-positive structures under down-regulation of CHC, APPL1, and EEA1.** Cells were transfected by siRNA for CHC (A and B), APPL1 (C and D) and EEA1 (E and F) for 48 h (see Materials and methods). Then fluorescently labeled Tf and EGF were internalized and chased as described in Fig. 6. Solid circles present the integral intensity of cargo colocalized with EEA1- (red), APPL1- (blue), and double APPL1+EEA1–positive endosomes (green). The control curves are presented by empty squares. Down-regulation of CHC, APPL1, and EEA1 was 95%, 70%, and 90%, respectively. Traffic of cargo in the control condition is repeatedly presented on panels A–F by empty squares. (G) Integral intensity of EGF colocalized with EEA1 under CHC knockdown (green) and APPL1 knockdown (blue). Sum of blue and green curves (sum of integral intensities of EGF colocalized with EEA1 upon APPL1 or CHC knockdown) is plotted by solid black circles. The time course of integral intensities of EGF colocalized with EEA1 for control is plotted by red squares.

delivery of EGF to the EEA1 compartment was 40% of control, the delivery to APPL1 was completely blocked (Fig. 7 B). Surprisingly, the delivery of EGF to the APPL1+EEA1 double compartment reached 65% of control, although the kinetics were delayed from 10 min (control) to 20 min (CHC knockdown). These results suggest that delivery of both Tf and EGF to APPL1-positive endosomes is clathrin dependent, whereas cargo can be delivered to the APPL1+EEA1 double compartment also by CIE. The kinetics of EGF in the CHC knockdown conditions supports the existence of a route from the EEA1 to the APPL1+EEA1 double compartment, in line with the live-cell imaging results (Fig. 5 E).

The partial knockdown of APPL1 caused fragmentation of APPL1 endosomes. Although the number of these endosomes increased by 25% (P = 0.038; Fig. S4 A), the amount of Tf in the APPL1 compartment decreased to 26% ± 6% of control at the maximum time point. The amount of Tf in the EEA1 endosomes was decreased to a similar level (29% ± 2%). However, the decrease of Tf in the APPL1+EEA1 compartment was much more pronounced (11% ± 2%) (Fig. 7 C). These results suggest that depletion of APPL1 has differential effects on the trafficking of Tf to APPL1, EEA1, and APPL1+EEA1 double-positive endosomes. In contrast, there were moderate alterations in amplitude (60% ± 30%) and slightly longer accumulation time for

the maximal amount of EGF in APPL1-positive endosomes. The delivery of EGF to EEA1 endosomes was decreased to the same level (59% ± 6%). Surprisingly, a comparison with the kinetics upon CHC knockdown revealed that the decrease of EGF delivery to EEA1-positive endosomes upon APPL1 knockdown mostly resulted from inhibition of CIE (Fig. 7 G). The strongest effect on EGF transport upon APPL1 knockdown was on the APPL1+EEA1 double-positive endosomes (35% ± 7%), similar to Tf transport (Fig. 7, E and F). This implies that cargo can be delivered to APPL1+EEA1 endosomes directly, without passing through APPL1 endosomes, in line with the observations by live cell imaging (Fig. 5 and Video 9). This result indicates that APPL1 is an essential component of APPL1- and APPL1+EEA1double-positive compartments.

Comparison of the time courses of EGF in the EEA1 compartment showed differential effects of CHC and APPL1 depletion on the kinetics of EGF delivery to EEA1 endosomes (Fig.7, B and D). Indeed, the kinetics under control conditions are the sum of two components, each revealed by the silencing of CHC and APPL1 (Fig. 7 G). The fact that each depletion condition suppresses one component without significantly affecting the other implies that the two components are independent. This supports the hypothesis of two kinetically distinct subpopulations of EEA1 endosomes postulated in model 2.

The knockdown of EEA1 (90%) decreased the number of EEA1 and APPL1+EEA1 endosomes to 20% and 12%, respectively, while increasing the number of APPL1-positive endosomes by 45% ± 11% relative to control. This led to a redistribution of cargo in APPL1-positive endosomes (Fig. 7, E and F). The total kinetics of Tf did not vary significantly, although it mostly involved APPL1-positive endosomes (∼50% colocalization of Tf with APPL1 at 3 min) at the expense of EEA1 and APPL1+EEA1 endosomes (22% and 18%, respectively). The characteristic recycling time of Tf increased from 10 ± 0.6 to 13 ± 0.6 min. In contrast, although at early stages EGF mostly redistributed to APPL1 (∼360% at point of maximum), at late stages it mostly left APPL1-positive endosomes and accumulated in few, large EEA1-positive and APPL1+EEA1 double-positive endosomes (Fig. 7 F).

Fitting model 2 to all perturbed conditions revealed that it could explain the measurements upon knockdown of CHC, APPL1, and EEA1 well (Figs. 8 D and S5) (see Mathematical methods). In contrast, the fit of model 1, A and B, to control and perturbed conditions was unsatisfactory (Fig. 8, B and C). In conclusion, model 2 best describes the kinetics of cargo transport through the three populations of early endosomes under normal and perturbed conditions.
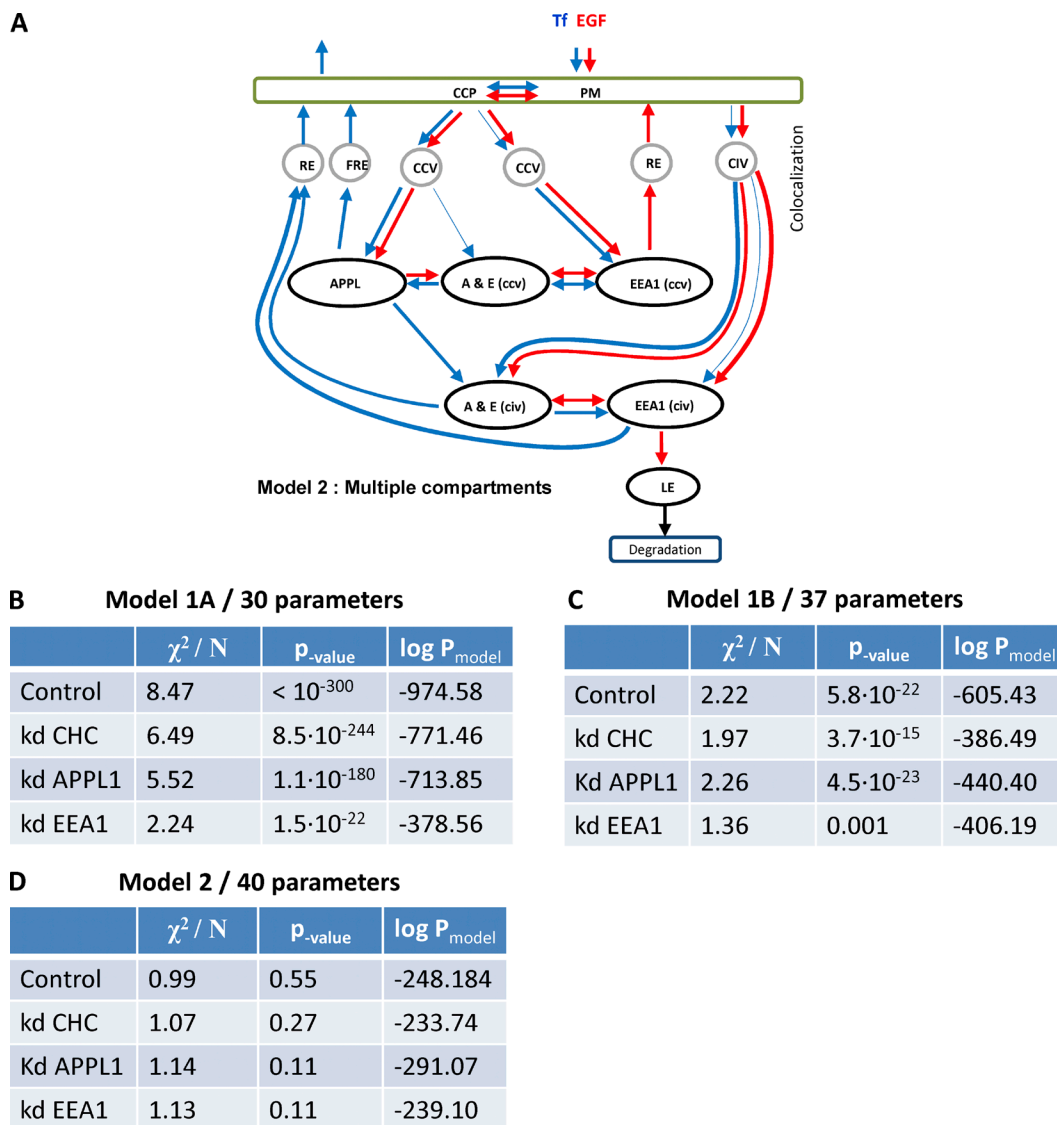
Discussion

In this study, we explored the structural and functional properties of the endosomal compartment labeled by the APPL1 protein and addressed the question of whether conversion of APPL1 vesicles into EEA1 endosomes (Zoncu et al., 2009) is the main mode of transport for endocytic cargo. First, we show that the APPL1-positive compartments are pleomorphic and consist of tubulo-vesicular structures typical of early endosomes. Inhibition of CDE does not reduce the number of APPL1 vesicles, suggesting that their biogenesis is not dependent on the flux of CCVs. Furthermore, APPL1 endosomes are stable over time, and they receive and sort distinct types of cargo with different

kinetics. They undergo fusion and fission and exchange cargo with EEA1 endosomes. Notably, APPL1-to-EEA1 conversion is very rare and not unidirectional, as EEA1 endosomes can also convert into APPL1 endosomes. The statistics of interactions of APPL1, EEA1, and APPL1+EEA1 endosomes suggest that the double-positive endosomes are not conversion intermediates but constitute a subpopulation of early endosomes with a specific role in cargo trafficking. Finally, the kinetics of Tf and EGF trafficking are inconsistent with a model in which the principal mode of transport of cargo from APPL1 to EEA1 vesicles occurs via conversion. We propose a new model for the organization of the early endocytic pathway in which APPL1 and APPL1+EEA1 endosomes represent a distinct population of early endosomes that receive and sort cargo in parallel with EEA1 endosomes.

Several lines of evidence support the idea that most APPL1 structures are bona fide early endosomes rather than vesicular intermediates in the biogenesis of EEA1 endosomes. In contrast to the study by Zoncu et al. (2009), inhibition of CDE failed to reduce the number or intensity of APPL1 structures. Beside technical issues, one possible explanation for this difference is that most of the experiments in that study were performed in cells overexpressing GFP- or mRFP-labeled APPL1 and EEA1, whereas in our experiments, with the exception of live cell imaging, we followed endogenous APPL1 and EEA1. We experienced problems with several EEA1-tagged constructs before succeeding in validating one that did not alter significantly the properties of the endosomal system. In addition, at least a fraction of APPL1 endosomes are long-lived entities (i.e., they retain APPL1 for much longer periods of time than the mean lifetime of CCV; Ehrlich et al., 2004; Kural et al., 2012). Ultrastructural analysis also revealed that the compartments harboring APPL1 have a tubulo-vesicular structure, characteristic of early endosomes. Their morphology is thus not typical of vesicular structures, such as uncoated CCVs. The tubules have a regular size, with a mean diameter of 49 ± 0.2 nm and variable length. Given the association of APPL1 with the tubules and the property of BAR (bin, amphiphysin, and Rvs161/167) domains in sensing or inducing membrane curvature (Gallop and McMahon, 2005), an obvious possibility is that APPL proteins themselves may shape the tubules. Finally, the presence of tubular structures is indicative of cargo sorting and indeed live cell imaging revealed events of cargo exit from APPL1 endosomes. The time course of EGF-to-Tf and Tf-to-EGF colocalization in the total endosomal pool (Fig. 6 D) and on APPL1 endosomes (Fig. 6 E) suggest that APPL1 endosomes have the ability to sort EGF and Tf. APPL1 endosomes also undergo complex membrane remodeling in the form of fusion, tubulation, and fission. The most frequently detected events were fusion and fission of APPL1-positive endosomes. The second-most-frequent events were fusion of APPL1 structures with, and budding from, APPL1+EEA1 endosomes. Importantly, our conclusions are corroborated by a recent study reporting APPL1-positive membranes containing internalized Fc receptor fusing with large preexisting (presumably EEA1-positive) early endosomes (Gan et al., 2013).

Our observations pose several questions concerning the mechanisms regulating the selective transport of cargo toward either compartment, how the two populations of endosomes communicate, and the functional requirement for APPL1 endosomes. The lifetimes of CCVs (between 35 and 400s; Ehrlich et al., 2004) and our measurements of the kinetics of

A

Tf EGF

Colocalization

Model 2 : Multiple compartments

CCP — PM

RE · FRE · CCV · CCV · RE · CIV

APPL · A & E (ccv) · EEA1 (ccv)

A & E (civ) · EEA1 (civ)

LE

Degradation

B   **Model 1A / 30 parameters**

	χ^2 / N	p$_{-value}$	log P$_{model}$
Control	8.47	$< 10^{-300}$	-974.58
kd CHC	6.49	$8.5 \cdot 10^{-244}$	-771.46
kd APPL1	5.52	$1.1 \cdot 10^{-180}$	-713.85
kd EEA1	2.24	$1.5 \cdot 10^{-22}$	-378.56

C   **Model 1B / 37 parameters**

	χ^2 / N	p$_{-value}$	log P$_{model}$
Control	2.22	$5.8 \cdot 10^{-22}$	-605.43
kd CHC	1.97	$3.7 \cdot 10^{-15}$	-386.49
Kd APPL1	2.26	$4.5 \cdot 10^{-23}$	-440.40
kd EEA1	1.36	0.001	-406.19

D   **Model 2 / 40 parameters**

	χ^2 / N	p$_{-value}$	log P$_{model}$
Control	0.99	0.55	-248.184
kd CHC	1.07	0.27	-233.74
Kd APPL1	1.14	0.11	-291.07
kd EEA1	1.13	0.11	-239.10

Figure 8. **Proposed models of cargo trafficking through APPL and EEA1 compartments.** (A) In model 2, cargo on PM follows either the clathrin pathway through CCPs to CCVs or the clathrin-independent route by CIVs. About 94% of Tf (blue) and 25% of EGF (red) follow CDE. Almost 75% of EGF and only 6% of Tf are internalized by CIVs. In line with model 1, A and B, we considered two pools of CCV that deliver cargo to APPL1-positive (36% EGF and 99.5%Tf) and EEA1-positive (64% EGF, 0.5%Tf) endosomes. The flux of Tf through CCV to EEA1 increased up to 22% by down-regulation of APPL1. The fit of model suggests that CIVs deliver cargo to APPL1+EEA1 and EEA1 endosomes. The dynamic of cargo traffic through EEA1-positive demonstrated complex behavior that cannot be explained in case of kinetically homogeneous compartments. The down-regulation of APPL1 and CHC revealed that cargo traffic consists of two components that can be separately inhibited. Therefore, we introduced in the model 2 two kinetically distinct EEA1 compartments, which we denote EEA1(ccv) and EEA1(civ) according to the main mode of cargo delivery. The corresponding double APPL1+EEA1 compartments were denoted A&E(ccv) and A&E(civ) accordingly. The sorting of cargo toward the recycling route occurs in the all three endocytic compartments APPL1, APPL1+EEA1, and EEA1. However, the delivery of EGF to the late endosomes (LE) and following degradation (~70% of EGF degrade in 30 min) occurs only through EEA1 compartment. We denote the recycling endosomes en route to PM and perinuclear recycling endosome in accordance to the kinetic rates of either fast recycling endosomes (FRE) or recycling endosomes RE. The thin arrows denote the routes that transport less than 10% of cargo from compartment, however the removal of them makes the fit to the experimental data unsatisfactory (P < 0.01). (B–D) Tables present results of the best fit of model 1A (B), model 1B (C), and model 2 (D) to the experimental data in control and perturbed cell. X^2/N denotes normalized χ^2:

$$\chi^2/N \;=\; \frac{1}{N}\sum_{i=1}^{N+1} \frac{(f_i - d_i)^2}{\sigma_i^2},$$

where f_i and d_i are model prediction and experimental data, σ_i is SEM of experimental data, N = 167. The p-values were calculated by χ^2 distribution. (B) The probability of null hypothesis that the deviation of the model prediction from the experiment is the result of random noise (p-value) is extremely low for all four conditions. Therefore, model 1A has to be rejected. (C) The probability of null hypothesis is very low for all conditions, although the logarithm of probability of model 1B (see Materials and methods) is much higher than those of 1A. Nevertheless, model 1B has to be rejected as well. (D) The probability of null hypothesis is high. Therefore, most probably the deviation of model 2 from the experiment is the result of experimental uncertainty. The model 2 is much more probable ln(P) > 100 than model 1B for all conditions. Therefore, the improvement of the quality of fit is statistically significant to justify three additional parameters.

cargo colocalization with APPL1 suggest that APPL1 endosomes receive cargo directly from CCVs, without the prior involvement of other endosomal compartments (Zoncu et al., 2009). Our detailed cargo trafficking measurements under knockdown of APPL1 and CHC suggest that APPL1 is required for cargo delivery by CDE and CIE. Interestingly, recent studies have also reported clathrin-dependent transport of EGF into EEA1 endosomes, bypassing APPL1 vesicles (Danson et al., 2013). The existence of parallel routes to APPL1 and EEA1 endosomes implies that cargo can be internalized into distinct early endosome types, thus adding to the complexity of the endocytic compartments (Mayor and Pagano, 2007; Leonard et al., 2008; Howes et al., 2010; Lim and Gleeson, 2011; Flores-Rodriguez et al., 2015). Cargo-sorting mechanisms could potentially operate at the level of cargo selection at the plasma membrane or as selective fusion of CCVs with APPL1 or EEA1 endosomes. For example, the CORVET complex has different functions in APPL1 and EEA1 endosomes (Perini et al., 2014), so it is possible that CCVs are also differentially tethered to the two types of endosomes. Whether EGF and Tf are internalized via the same CCVs is still a matter of debate, although the large structural heterogeneity of CCVs may reflect a functional specialization (Cheng et al., 2007; Saffarian et al., 2009). For example, G protein–coupled receptors are endocytosed via a distinct subpopulation of CCPs (Puthenveedu and von Zastrow, 2006). Moreover, immunoelectron microscopy data favor the notion of largely separate CCPs and CCVs trafficking of Tf or EGF (Tosoni et al., 2005). The gradual increase in EGF-to-Tf colocalization over the first 10–15 min after the pulse (Fig. 6 D) would be consistent with the existence of distinct vesicles (derived from CDE or CIE) for EGF and Tf uptake that nevertheless deliver their content to common APPL1 endosomes. Our analysis also demonstrates that APPL1 endosomes receive less Tf and EGF than EEA1 endosomes. However, it is possible that other cargo molecules could be preferentially directed toward APPL1 endosomes via specific CCVs or other clathrin-independent vesicles. In addition, differences in the spatial distribution and number of APPL1 and EEA1 endosomes alone could determine different rates of cargo transport.

With respect to trafficking between APPL1 and EEA1 endosomes, the 30% colocalization between these markers suggests that a significant fraction of both compartments is involved in cargo exchange at any given time. In the APPL1+EEA1 endosomes, both Rab5 effectors could be recruited independently or, alternatively, the two compartments might undergo fusion resulting in a hybrid compartment. However, such events are much more infrequent than, for example, the fusion of APPL1 with preexisting double-positive endosomes. We did observe APPL1-to-EEA1 conversion events, but such events were very rare (5%). This is consistent with previous studies, where only a small percentage (<10%) of APPL endosomes were reported to convert into EEA1 endosomes (Zoncu et al., 2009). The shedding of APPL1 may be more representative of macropinosomes (Zoncu et al., 2009). However, we also observed the opposite phenomenon, namely the conversion of EEA1 into APPL1-positive endosomes (7%). Our results therefore argue that APPL1 endosomes are much more dynamic than previously thought, exchanging identity and cargo bi-directionally with EEA1 endosomes.

To develop a new model of cargo traffic through the early endocytic pathway we used a system identification approach. First, we performed a detailed kinetic analysis of EGF and Tf transport through APPL1, APPL1+EEA1, and EEA1 endosomes under control and perturbed conditions. Second we developed a set of mathematical models based on data from the literature (Fig.1, A and B) and tested whether they could explain the measured kinetics. This was not the case and, based on the time course of EGF accumulation in the EEA1 compartments (see control vs. CHC and APPL1 knockdown; Fig. 7), we had to introduce two kinetically distinct sub-populations of EEA1 and APPL1+EEA1 endosomes. Indeed, endosome with different kinetics properties have been reported by Lakadamyali et al. (2006). Note that these endosomes do not need to be molecularly distinct. They may simply have a different density of tethering machineries, endosome size, motility patterns, and other features. The resulting model 2 (Fig. 8 A) was the simplest model able to explain the experimental data (i.e., based on the quantitative Occam's razor principle [Sivia and Carlile, 1992], there is no need to invoke additional compartments and kinetic rates). The model not only describes well the experimental transport kinetics but also makes predictions on the flux of cargo through the endosomal compartments. First, the APPL1 compartment has different rates of EGF and Tf traffic and, as such, must have cargo-sorting ability. Second, a large volume of cargo transport traverses the APPL1 compartment. Although we detected a maximum of 20% of Tf colocalized to APPL1, more than 85% passes through APPL1 endosomes. Third, most APPL1 endosomes bi-directionally interact with APPL1+EEA1 endosomes. The latter compartment therefore plays a key role in the traffic of cargo between APPL1 and EEA1 endosomes.

Because several studies have reported interactions of APPL1 with specific receptors and components of signaling pathways (Schenck et al., 2008; Deepa and Dong, 2009; Majumdar et al., 2011; Xin et al., 2011; Hupalowska et al., 2012), APPL1 endosomes could play a specialized function in the trafficking of cargo devoted to signal transduction. The lower capacity of APPL1 endosomes for cargo trafficking in comparison to EEA1 endosomes suggests that they are not involved in bulk endocytosis. Trafficking of signaling cargo into APPL1 endosomes might temporarily protect signaling complexes from entering the route to degradation, thus regulating the signaling processes not only spatially but also temporally. This possibility is supported by our data showing that at later time points the proportion of cargo in APPL1+EEA1 endosomes increased. Other supportive evidence comes from the partial knockdown of EEA1, which led to decreased residence time of EGF within the endocytic system (Fig. 7 F). Model 2 explained this effect by the predominant loss of APPL1+EEA1 endosomes (Fig. S4 A). In agreement with this idea, extended residence of EGF in APPL1 endosomes has been shown to affect ERK activation downstream of EGFR (Zoncu et al., 2009). It is also possible that certain extra- or intracellular cues (e.g., signaling events, metabolic changes) could change the proportion of cargo flow between APPL1 and EEA1 endosomes.

Accumulating evidence indicates that endosomal compartments play active roles in intracellular signal transduction, regulating in time and space its range and outcome (Sadowski et al., 2009; Sorkin and von Zastrow, 2009). Moreover, it is becoming clear that the initial categorization of endocytic compartments into early, late, and recycling endosomes is oversimplified and a larger variety of endosomal structures exist in various cell types (Perret et al., 2005; Bökel et al., 2006; Hayakawa et al., 2006; Lakadamyali et al., 2006). Understanding the properties of APPL1 endosomes in relation to other endocytic routes should reveal new principles whereby cells coordinate trafficking and signaling functions.

Materials and methods

Cell culture and transfection
HeLa cells were cultured in MEM with 10% fetal bovine serum, 100 U/ml penicillin, 100 µg/ml streptomycin, and 2 mM glutamine (all reagents from Sigma-Aldrich) at 37°C with 5% CO_2. Cells were transiently transfected with appropriate plasmids using FuGENE 6 (Roche Diagnostics) and analyzed 24 h after transfection. Cells were incubated with or without 80 µM Dynasore (Sigma-Aldrich) for 60 min in DMEM/Hepes (Thermo Fisher Scientific) at 37°C. Cells internalized fluorescent transferrin during the last 10 min of the incubation with the drug.

Knockdown of clathrin
The following siRNA oligonucleotides against clathrin heavy chain were used: 5′-AAGCUGGGAAAACUCUUCAGA-3′, chc-1 (Motley et al., 2003) transfected at 10 nM final concentration or the pair of two oligonucleotides corresponding to the sequences 5′-GAAAGAATCTGTAGAGAAA-3′ and 5′-GCAATGAGCTGTTTGAAGA-3′ transfected at 50 nM each, as described elsewhere (Chen and De Camilli, 2005). All oligonucleotides were synthesized by Ambion (Thermo Fisher Scientific) and together with the negative control siRNA (Ambion 4611) were transfected using HiPerFect (Qiagen) for 48 h before the analysis. APPL1 and EEA1 were depleted using endoribonuclease-prepared siRNA (esiRNA), produced and purified as described elsewhere (Kittler et al., 2005). In brief, optimal esiRNA 400–600 bp target regions were selected within a gene of interest using the DEQOR web server (Henschel et al., 2004). The selected region was first amplified from HeLa cDNA with specific primers that contained a T7 promoter sequence (underlined): APPL1 forward, 5′-TCACTATAGGGAGAGCCCTCTCTCTAGATTCTC-3′, APPL1 reverse, 5′-TCACTATAGGGAGACACATATCTTTTCCCCC-3′; EEA1 forward, 5′-TCACTATAGGGAGAGCACAAGACCGTGTCC-3′, EAA1 reverse, 5′-TCACTATAGGGAGACAGATCTTGCAAAGCCTGC-3′; negative control β-gal forward, 5′-TCACTATAGGGAGAGGCTGGCGTAATAGCGAAGAG-3′, β-gal reverse, 5′-TCACTATAGGGAGACCATTAAAGCGAGTGGCAACA-3′. A product of the first PCR served as a template for the second PCR step using T7 promoter primers. This tagged cDNA fragment was reverse-transcribed to long double-stranded RNA and digested to short <30 base pair fragments using limited digestion with RNase III. esiRNA was purified, precipitated, and reconstituted in RNase-free water. esiRNAs were transfected at 33 nM using HiPerFect for 48 h before the analysis.

Cell lysis and Western blot
48 h after transfection with siRNA, cells were lysed in PBS containing 1% Triton X-100, 0.1% SDS, and protease inhibitors (6 µg/ml chymostatin, 0.5 µg/ml leupeptin, 10 µg/ml antipain, 2 µg/ml aprotinin, 0.7 µg/ml pepstatin, and 10 µg/ml amidinophenyl-methanesulfonyl fluoride; Sigma-Aldrich). The protein concentration of lysates was determined by using the BCA protein assay (Pierce; Thermo Fisher Scientific) with BSA as a standard. Cell lysates were then separated by 8% SDS-PAGE and transferred to nitrocellulose membrane. The membrane was blocked in 5% milk in PBS containing 0.1% Tween and probed with rabbit sera against APPL1, EEA1 (Miaczynska et al., 2004), and Rab5 (Abcam) or mouse monoclonal antibody against clathrin heavy chain (BD Biosciences). After washing, membranes were incubated with HRP-conjugated goat anti-rabbit or anti-mouse IgG (Jackson ImmunoResearch Laboratories), washed in PBS containing 0.1% Tween, incubated with electrochemiluminescence reagent, and exposed to an x-ray film.

Pulse-chase internalization assays
HeLa cells grown on glass coverslips were serum-starved overnight and incubated in CO_2-independent medium (Invitrogen) with 0.2% BSA for 2 h before the internalization assay.

For the microscopy-based readouts, cells were labeled at 37°C by a 30-s pulse of Tf-Alexa647 (20 µg/ml; Invitrogen) and EGF-Oregon green (1 µg/ml; Invitrogen) in CO_2-independent medium and chased for 1.5 min in a serum-free medium, followed by chase in a medium containing 200 µg/ml unlabeled holo-Tf (Sigma-Aldrich) for the indicated times. Cells were fixed and processed for immunofluorescence with rabbit anti-APPL1 (Miaczynska et al., 2004) and mouse anti-EEA1 (BD Biosciences), followed by Alexa568- and Alexa405-labeled secondary antibodies, respectively. Ten images (12-bit pixel depth) per each time point were taken using a confocal microscope (Leica TCS SP2 with AOBS) with a 63x/1.4 NA oil immersion objective, 200-Hz speed, and 1024 × 1024 pixel resolution. Four fluorescent channels were imaged sequentially. Alexa405 was excited with a 405-nm diode laser, Oregon green with a 514-nm argon laser line, Alexa568 with a 543-nm helium-neon laser line and Alexa647 was excited with 633-nm helium-neon laser line. Images were exported as TIFF files directly into the Motiontracking software and served as a basis for quantitative analysis.

For biochemical readouts, cells were labeled at 37°C by a 30-s pulse of biotinylated Tf (10 µg/ml; Sigma-Aldrich) and chased for 1.5 min in a serum-free medium, followed by chase in a medium containing 200 µg/ml unlabeled holo-Tf (Sigma-Aldrich) for indicated times. At the end of chase periods, cells were acid washed (MEM titrated to pH 3.5) for 2.5 min on ice to remove surface-bound ligand, then washed twice with ice-cold PBS and lysed in PBS containing 1% Triton X-100, 0.1% SDS, and protease inhibitors (6 µg/ml chymostatin, 0.5 µg/ml leupeptin, 10 µg/ml antipain, 2 µg/ml aprotinin, 0.7 µg/ml pepstatin, and 10 µg/ml amidinophenyl-methanesulfonyl fluoridec; Sigma-Aldrich). The protein concentration of lysates was determined using the BCA protein assay with BSA as a standard.

Electrochemiluminescence assay for detection of biotinylated Tf
The content of biotinylated Tf in cell lysates was measured in an electrochemiluminescence-based assay using Meso Scale Discovery (MSD) technology platform. The extracts were applied to avidine-coated standard plates (MSD) for 1 h on a shaker platform, followed by addition of streptavidin SULFO-TAG (R32AD-1; MSD) for 1 h and three washes with MSD Tris wash buffer (R61TX-1). Afterwards, the MSD Read Buffer (R92TC-2) was added and electrochemiluminescence of the samples was read in the SECTOR Imager 2400 (MSD).

Immunofluorescence
HeLa cells grown on 12-mm round glass coverslips were fixed in 3% paraformaldehyde in PBS for 12 min and permeabilized for 10 min with PBS containing 0.1% wt/vol saponin, 0.2% wt/vol gelatin, and 5 mg/ml BSA. Mouse monoclonal antibodies against the following proteins were used: EEA1, LAMP1, and GM130 (BD Biosciences), α-adaptin (BD Biosciences), γ-adaptin (Sigma-Aldrich), and clathrin heavy chain (Affinity Bioreagents), combined with rabbit polyclonal anti-APPL1 (Miaczynska et al., 2004) in PBS containing 0.2% gelatin and 0.01% saponin for 30 min. Cells were washed and incubated with Alexa-labeled secondary antibodies for 30 min. After additional washes, samples were mounted with Mowiol (Sigma-Aldrich) on glass slides and examined with laser scanning confocal microscope (TCS SP2 with *acousto-optical beam splitter; Leica*) using a 63x/1.4 NA oil immersion objective (8-bit images of 1024 × 1024–pixel resolution). Presented figures were assembled using Photoshop 7.0 (Adobe) with brightness and contrast adjustment and 0.5-pixel Gaussian blur.

Electron microscopy
HeLa cells in 3 cm dishes were fixed in PBS containing 1% PFA/0.1% glutaraldehyde and 0.01% digitonin for 15 min at RT and then with 1% PFA in PBS for further 15 min. They were then washed and incubated with 50 mM glycine in PBS for 5 min and then with blocking solution

(1% BSA, 0.1% digitonin, and 50 mM glycine in PBS) before incubation with rabbit anti-APPL1 diluted 1:100 in 0.2% BSA, 0.1% fish skin gelatin for 60 min at RT. After washing (6 × 10 min with PBS) cells were incubated with 1.4 nm goat anti-rabbit Nanogold (Nanoprobes) for 2 h at RT. After fixation for 5 min with 1% glutaraldehyde in PBS, cells were washed sequentially with PBS and then distilled water (3 × 5 min) before silver enhancement for 3 min at RT in the dark according to the manufacturer's instructions (Nanoprobes HQ Silver). Cells were further processed following standard procedures and flat embedded in epon resin. Sections were cut parallel to the culture substratum and stained with uranyl acetate and lead citrate before viewing.

Live imaging

HeLa cells were transiently transfected using DreamFect Gold reagent (OZ BioSciences) or Effectene (Qiagen) for 24 h with plasmids pEG-FP-C3-APPL1 (Miaczynska et al., 2004), pEGFP-C3-Rab5 (Sönnichsen et al., 2000), mRFP-human APPL (a gift from P. De Camilli [Addgene plasmid 22202]) or tagRFP-T-EEA1 (a gift from S. Corvera, University of Massachusetts Medical School, Worcester, MA [Addgene plasmid 42635]) and analyzed 24 h after transfection. Alexa555-labeled cargo (EGF or Tf) were obtained from Invitrogen. A 2-min pulse of cargo (EGF: 1 µg/ml, Tf: 25 µg/ml) was given to the cells under the microscope at 37° using a perfusion chamber. Then cells were imaged by time-lapse microscopy (Spinning Disc, Andor-Olympus-IX71 inverted stand microscope and Nikon TiE inverted stand microscope equipped with spinning disc scan head [CSU-X1; Yokogawa], fast piezo objective z-positioner [Physik Instrumente], and back-illuminated EMCCD camera [iXon EM+ DU-897 BV; Andor]). Imaging was done with an Olympus UPlanSApo 100x 1.4 Oil and Nikon Apo 100x 1.49 Oil DIC 0.13–0.20 objectives (illumination by lasers: DPSS-488nm, DPSS-561nm, DPSS-640nm) during 10–15 min of the chase time. Individual planes were recorded (7–10 frames per second). Z-stacks of three planes (step 1 µm) were recorded two to three times per second. Three-color images were recorded with one confocal plane, 2.5 frames per second. Individual vesicles were found and tracked by Motiontracking software (Rink et al., 2005; Collinet et al., 2010).

Mathematical methods

Model 1A: APPL-positive endosomes as an intermediate for APPL-to-EEA1 conversion. The conversion model envisages that APPL vesicles acquire EEA1 either directly by forming a short-living double-positive APPL1+EEA1 intermediate, and subsequently losing APPL1, thus generating EEA1-positive early endosomes, or indirectly through PI(3)P-positive APPL1- and EEA1-negative intermediate, which later convert to EEA1 endosomes (Zoncu et al., 2009). This model has the following implications: (a) The existence of intermediate vesicles with competitive exchange of APPL to EEA1 implies that the delivery rate from APPL1 vesicles to EEA1 endosomes must be the same for different types of cargo (i.e., EGF and Tf in our experimental setup) and (b) there is no retrograde flux of cargo from EEA1 to APPL1 compartments. Because it was reported that EGF and Tf enter cells mainly transported by different CCVs (Stang et al., 2004; Tosoni et al., 2005), and that a significant fraction of EGF enters via a clathrin-independent pathway (Sigismund et al., 2005, 2008), we considered distinct rates of vesicular transport from plasma membrane to APPL1 endosomes for both types of cargo. We also considered different rates for sorting of EGF and Tf from EEA1 endosomes to recycling endosomes (RE) and late endosomes (LE). In contrast, for the steps required for the APPL-to-EEA1 conversion (Zoncu et al., 2009) we assigned the same rates for both types of cargo. Because the properties of PI(3)P-positive EEA1-negative intermediates are poorly characterized, we included the possibility of cargo recycling from this endosomes in the model. Tf is internalized in the form of holo-transferrin and recycled to the plasma membrane (PM) in the form of apo-transferrin. Because the affinity of holo-transferrin and apo-transferrin to the receptor TFR differs ∼30 fold (Dautry-Varsat et al., 1983), we considered apo-transferrin on the PM as a separate entity (*Tf_apo*). To ensure that the ratio between direct conversion of APPL1- to EEA1-positive endosomes and conversion through PI(3)P-positive endosomes is 1–5 as reported by Zoncu et al. (2009), we added a constrain on the rate ratio: $k_{appl->pi3p} = 5 \cdot k_{appl->e+a}$. We formally included equal number of steps in the cargo traffic model for both types of cargo with the idea that fitting will set the rates for the unlikely or low efficiency steps (e.g., uptake of Tf by clathrin-independent pathways, degradation of Tf, etc.) to zero. The same logic was applied to the other models (model 1B and model 2). The resulting model consisted of 29 ODEs with 31 independent rates (see models zip file [Model1a-fix] in the online supplemental material).

As expected, the rates of Tf traffic to degradation were fitted to zero. Removal of these "dead end" steps resulted in model 1A (Fig.1 A), which was described by the following set of 26 ODEs with 29 independent rates (see supplemental models zip file: Model1a-fix):

$$\frac{dC_{pm}^{EGF}}{dt} = \Phi_{medium}^{EGF}(t) - \left(k_{pm->ccp}^{EGF} + k_{pm->civ}^{EGF}\right)C_{pm}^{EGF} + k_{fre->pm}^{EGF}C_{fre}^{EGF} \quad (1)$$

$$\frac{dC_{ccp}^{EGF}}{dt} = k_{pm->ccp}^{EGF}C_{pm}^{EGF} - \left(k_{ccp->ccv_1}^{EGF} + k_{ccp->ccv_2}^{EGF}\right)C_{ccp}^{EGF} \quad (2)$$

$$\frac{dC_{ccv_1}^{EGF}}{dt} = k_{ccp->ccv_1}^{EGF}C_{cpp}^{EGF} - k_{ccv_1->appl}^{EGF}C_{ccv_1}^{EGF} \quad (3)$$

$$\frac{dC_{ccv_2}^{EGF}}{dt} = k_{ccp->ccv_2}^{EGF}C_{cpp}^{EGF} - k_{ccv_2->eea1}^{EGF}C_{ccv_2}^{EGF} \quad (4)$$

$$\frac{dC_{civ}^{EGF}}{dt} = k_{pm->civ}^{EGF}C_{ccp}^{EGF} - k_{civ->eea1}^{EGF}C_{civ}^{EGF} \quad (5)$$

$$\frac{dC_{appl}^{EGF}}{dt} = k_{ccv_1\_appl}^{EGF}C_{ccv_1}^{EGF} - \left(k_{appl->e+a} + k_{appl->pi3p}\right)C_{appl}^{EGF} \quad (6)$$

$$\frac{dC_{e+a}^{EGF}}{dt} = k_{appl->e+a}^{EGF}C_{appl}^{EGF} - k_{e+a->eea1}C_{e+a}^{EGF} \quad (7)$$

$$\frac{dC_{pi3p}^{EGF}}{dt} = k_{appl->pi3p}C_{appl}^{EGF} - \left(k_{pi3p->eea1} + k_{pi3p->fre}^{EGF}\right)C_{pi3p}^{EGF} \quad (8)$$

$$\frac{dC_{eea1}^{EGF}}{dt} = k_{ccv_2->eea1}^{EGF}C_{ccv_2}^{EGF} + k_{civ->eea1}^{EGF}C_{civ}^{EGF} + k_{e+a->eea1}C_{e+a}^{EGF+} \\ k_{pi3p->eea1}C_{pi3p}^{EGF} - \left(k_{eea1->re}^{EGF} + k_{eea1->le}^{EGF}\right)C_{eea1}^{EGF} \quad (9)$$

$$\frac{dC_{le}^{EGF}}{dt} = k_{eea1->le}^{EGF}C_{eea1}^{EGF} - k_{deg}C_{le}^{EGF} \quad (10)$$

$$\frac{dC_{re}^{EGF}}{dt} = k_{eea1->re}^{EGF}C_{eea1}^{EGF} - k_{re->pm}^{EGF}C_{re}^{EGF} \quad (11)$$

$$\frac{dC_{fre}^{EGF}}{dt} = k_{pi3p->fre}^{EGF}C_{pi3p}^{EGF} - k_{fre->pm}^{EGF}C_{fre}^{EGF} \quad (12)$$

$$\frac{dC_{deg}^{EGF}}{dt} = k_{deg}^{EGF}C_{le}^{EGF} \quad (13)$$

$$\frac{dC^{Tf}_{pm}}{dt} = \Phi^{Tf}_{medium}(t) - \left(k^{Tf}_{pm\to out} + k^{Tf}_{pm\to ccp} + k^{Tf}_{pm\to civ}\right)C^{Tf}_{pm} \tag{14}$$

$$\frac{dC^{Tf\_apo}_{pm}}{dt} = k^{Tf}_{fre\to pm} C^{Tf}_{fre} + k^{Tf}_{re\to pm} C^{Tf}_{re} - k^{Tf\_apo}_{pm\to out} C^{Tf\_apo}_{pm} \tag{15}$$

$$\frac{dC^{Tf}_{ccp}}{dt} = k^{Tf}_{pm\to ccp} C^{Tf}_{pm} - \left(k^{Tf}_{ccp\to ccv_1} + k^{Tf}_{ccp\to ccv_2}\right)C^{Tf}_{ccp} \tag{16}$$

$$\frac{dC^{Tf}_{ccv_1}}{dt} = k^{Tf}_{ccp\to ccv_1} C^{Tf}_{ccp} - k^{Tf}_{ccv_1\to appl} C^{Tf}_{ccv_1} \tag{17}$$

$$\frac{dC^{Tf}_{ccv_2}}{dt} = k^{Tf}_{ccp\to ccv_2} C^{Tf}_{ccp} - k^{Tf}_{ccv_2\to eea1} C^{Tf}_{ccv_2} \tag{18}$$

$$\frac{dC^{Tf}_{civ}}{dt} = k^{Tf}_{pm\to civ} C^{Tf}_{pm} - k^{Tf}_{civ\to eea1} C^{Tf}_{civ} \tag{19}$$

$$\frac{dC^{Tf}_{appl}}{dt} = k^{Tf}_{ccv_1\to appl} C^{Tf}_{ccv_1} - \left(k_{appl\to e+a} + k_{appl\to pi3p}\right)C^{Tf}_{appl} \tag{20}$$

$$\frac{dC^{Tf}_{e+a}}{dt} = k_{appl\to e+a} C^{Tf}_{appl} - k_{e+a\to eea1} C^{Tf}_{e+a} \tag{21}$$

$$\frac{dC^{Tf}_{pi3p}}{dt} = k_{appl\to pi3p} C^{Tf}_{appl} - \left(k_{pi3p\to eea1} + k^{Tf}_{pi3p\to fre}\right)C^{Tf}_{pi3p} \tag{22}$$

$$\frac{dC^{Tf}_{eea1}}{dt} = k^{Tf}_{civ\to eea1} C^{Tf}_{civ} + k^{Tf}_{civ_2\to eea1} C^{Tf}_{ccv_2} + k_{e+a\to eea1} C^{Tf}_{e+a} + k_{pi3p\to eea1} C^{Tf}_{pi3p} - k^{Tf}_{eea1\to re} C^{Tf}_{eea1} \tag{23}$$

$$\frac{dC^{Tf}_{re}}{dt} = k^{Tf}_{eea1\to re} C^{Tf}_{eea1} - k^{Tf}_{re\to pm} C^{Tf}_{re} \tag{24}$$

$$\frac{dC^{Tf}_{fre}}{dt} = k^{Tf}_{pi3p\to fre} C^{Tf}_{pi3p} - k^{Tf}_{fre\to pm} C^{Tf}_{fre} \tag{25}$$

$$\frac{dC^{Tf}_{out}}{dt} = k^{Tf}_{pm\to out} C^{Tf}_{pm} + k^{Tf\_apo}_{pm\to out} C^{Tf\_apo}_{pm} \tag{26}$$

In those equations, $\Phi^{Tfn}_{medium}(t)$ and $\Phi^{EGF}_{medium}(t)$ are cargo unit pulse functions. They are equal to 1.0 in the time interval from −0.5 min to 0.0 min, and equal to zero everywhere else. The rational for this choice of loading function is as follows: The high concentration of EGF (1000 ng/ml, molecular mass = 6 kD) and Tf (25 µg/ml, molecular mass = 80 kD) results in a mean distance between the molecules of $l \sim 100$ nm. The diffusion coefficient for small proteins is in the range of 10 µ²/s. This gives the characteristic diffusion time as

$$t \sim \frac{l^2}{D} = 10^{-3}\ \text{s}.$$

Therefore, in a time scale of seconds (the pulse duration is 30 s), we can assume that the loading rate is constant during the pulse time.

In the equations, the superscript index specifies cargo, either *EGF* or *Tf* and *Tf_apo*, and the subscript index specifies either the compartment containing the amount of cargo *C* or the direction of transition from one compartment to another for the rate constant *k*. The list of subscript indexes is: (a) *pm*, plasma membrane; (b) *ccp*, clathrin-coated pits;

(c) *ccv₁*, clathrin-coated vesicles delivered to APPL1 endosomes; (d) *ccv₂*, clathrin-coated vesicles delivered to EEA1 endosomes; (e) *appl*, APPL1-positive endosomes; (f) *pi3p*, PI(3)P-positive EEA1-negative endosomes en route from APPL1 to EEA1; (g) *e+a*, double EEA1+APPL1–positive endosomes; (h) *eea1*, EEA1-positive endosomes; (i) *re*, recycling endosomes (perinuclear recycling endosome and recycling vesicles); (j0) *fre*, fast recycling vesicles; (k) *le*, late endosomes; (l) *deg*, degradation; and (m) *out*, release into the medium.

For example, C^{EGF}_{pm} denotes the amount of EGF at the plasma membrane, $k^{Tf}_{ccv_1\to appl}$ denotes the rate of Tf delivery from CCV₁ to APPL1 endosomes, $k^{Tf}_{pm\to out}$ denotes the rate of Tf release into the medium. The rates, which have to be equal for both cargoes as a result of conversion have not superscript (e.g., $k_{appl\to e+a}$ in models 1A and 1B).

In model 1A, Eqs. 1, 2, 14, 15, and 16 describe all steps responsible for cargo balance at the plasma membrane: binding of cargo from medium to receptors at the plasma membrane, migration to CCP, internalization (via CDE and CIE) and recycling back to the plasma membrane. Eqs. 3, 4, 17, and 18, describe cargo flux through CCV. Eqs. 5 and 19 describe clathrin-independent internalization of cargo. Eqs. 6 and 20 describe the steps responsible for cargo balance at APPL1-positive endosomes: delivery of cargo by CCV and exit either by direct conversion through double APPL1+EEA1 endosomes or indirectly through PI(3)P-positive EEA1-negative endosomes. Eqs. 7 and 21 describe cargo flux through APPL1+EEA1–positive endosomes toward EEA1-positive endosomes. It includes delivery from APPL1-positive endosomes and exit toward EEA1-positive endosomes by loss of APPL1. The flux through PI(3)P-positive EEA1-negative endosomes is described by Eqs. 8 and 22. In contrast to APPL1+EEA1 intermediate, these endosomes considered to be formed by the loss of APPL1 and are able for cargo sorting toward recycling route. Eqs. 9 and 23 describe cargo sorting in EEA1-positive endosomes. Eq. 10 describes EGF delivery from EEA1 endosomes to late endosomes and its consequent degradation (i.e., decay of fluorescence). Eqs. 11 and 24 describe cargo flux through recycling endosomes by sorting from EEA1-positive endosomes and recycling to the plasma membrane. The fast recycling is described by Eqs. 12 and 25. Eqs. 13 and 26 are used to calculate integral of degraded (13) and recycled (26) cargo.

Model 1B: 40% of APPL-positive endosomes constitute a stable endocytic compartment. In model 1B, we assumed that 40% of APPL1 endosomes constitute a stable compartment, capable of cargo sorting and bi-directional exchange with EEA1 endosomes through the formation of a double APPL1+EEA1 intermediate. The model was described by 32 ODEs with 43 independent rates (see supplemental models zip file: Model1b). Three additional constrains ($k_{appl\to pi3p} = 5 \cdot k_{appl\to e+a}$, $k_{ccv_1\to appl^*} = 0.667 \cdot k_{ccv_1\to appl}$, $k^{Tf}_{ccv_1\to appl^*} = 0.667 \cdot k^{Tf}_{ccv_1\to appl}$) ensured the ratio between routes through the direct conversion APPL1 to EEA1 (10%), indirect conversion (through PI(3)P endosomes) (50%) and stable APPL1 endosomes (40%). After we fitted the model to the data, seven rates were fitted to zero (e.g., back flux of EGF from stable APPL1+EEA1–positive endosomes to stable APPL1-positive endosomes, Tf traffic to degradation), and the resulting model 1B has only 36 independent rates (supplemental models zip file: Model1b-fix):

$$\frac{dC^{EGF}_{pm}}{dt} = \Phi^{EGF}_{medium}(t) - \left(k^{EGF}_{pm\to cpp} + k^{EGF}_{pm\to civ}\right)C^{EGF}_{pm} + k^{EGF}_{fre\to pm} C^{EGF}_{fre} \tag{27}$$

$$\frac{dC^{EGF}_{ccp}}{dt} = k^{EGF}_{pm\to ccp} C^{EGF}_{pm} - \left(k^{EGF}_{ccp\to ccv_1} + k^{EGF}_{ccp\to ccv_2}\right)C^{EGF}_{ccp} \tag{28}$$

$$\frac{dC^{EGF}_{ccv_1}}{dt} = k^{EGF}_{ccp\to ccv_1} C^{EGF}_{cpp} - \left(k^{EGF}_{ccv_1\to appl} + k^{EGF}_{ccv_1\to appl^*}\right)C^{EGF}_{ccv_1} \tag{29}$$

$$\frac{dC_{ccv_2}^{EGF}}{dt} = k_{ccp->ccv_2}^{EGF} C_{ccp}^{EGF} - k_{ccv_2->eea1}^{EGF} C_{ccv_2}^{EGF} \tag{30}$$

$$\frac{dC_{civ}^{EGF}}{dt} = k_{pm->civ}^{EGF} C_{ccp}^{EGF} - k_{civ->eea1}^{EGF} C_{civ}^{EGF} \tag{31}$$

$$\frac{dC_{appl}^{EGF}}{dt} = k_{ccv_1\_appl}^{EGF} C_{ccv_1}^{EGF} - \left(k_{appl->e+a} + k_{appl->pi3p}\right) C_{appl}^{EGF} \tag{32}$$

$$\frac{dC_{e+a}^{EGF}}{dt} = k_{appl->e+a} C_{appl}^{EGF} - k_{e+a->eea1} C_{e+a}^{EGF} \tag{33}$$

$$\frac{dC_{pi3p}^{EGF}}{dt} = k_{appl->pi3p} C_{appl}^{EGF} - k_{pi3p->eea1} C_{pi3p}^{EGF} \tag{34}$$

$$\frac{dC_{appl^*}^{EGF}}{dt} = k_{ccv_1->appl^*}^{EGF} C_{ccv_1}^{EGF} - k_{appl^*->e+a^*}^{EGF} C_{appl^*}^{EGF} \tag{35}$$

$$\frac{dC_{e+a^*}^{EGF}}{dt} = k_{appl^*->e+a}^{EGF} C_{appl^*}^{EGF} + k_{eea1->e\_a^*}^{EGF} C_{eea1}^{EGF} - k_{e+a^*->eea1}^{EGF} C_{e+a}^{EGF} \tag{36}$$

$$\frac{dC_{eea1}^{EGF}}{dt} = k_{ccv_2->eea1}^{EGF} C_{ccv_2}^{EGF} + k_{civ->eea1}^{EGF} C_{civ}^{EGF} + k_{e+a->eea1} C_{e+a}^{EGF} + k_{e+a^*->eea1} C_{e+a^*}^{EGF} + k_{pi3p->eea1} C_{pi3p}^{EGF} - \left(\begin{matrix} k_{eea1->e+a^*}^{EGF} + \\ k_{eea1->re}^{EGF} + k_{eea1->le}^{EGF} \end{matrix}\right) C_{eea1}^{EGF} \tag{37}$$

$$\frac{dC_{le}^{EGF}}{dt} = k_{eea1->le}^{EGF} C_{eea1}^{EGF} - k_{deg} C_{le}^{EGF} \tag{38}$$

$$\frac{dC_{re}^{EGF}}{dt} = k_{eea1->re}^{EGF} C_{eea1}^{EGF} - k_{re->pm}^{EGF} C_{re}^{EGF} \tag{39}$$

$$\frac{dC_{deg}^{EGF}}{dt} = k_{deg}^{EGF} C_{le}^{EGF} \tag{40}$$

$$\frac{dC_{out}^{EGF}}{dt} = k_{pm->out}^{EGF} C_{pm}^{EGF} \tag{41}$$

$$\frac{dC_{pm}^{Tf}}{dt} = \Phi_{medium}^{Tf}(t) - \left(k_{pm->out}^{Tf} + k_{pm->ccp}^{Tf} + k_{pm->civ}^{Tf}\right) C_{pm}^{Tf} \tag{42}$$

$$\frac{dC_{pm}^{Tf\_apo}}{dt} = k_{fre->pm}^{Tf} C_{fre}^{Tf} + k_{re->pm}^{Tf} C_{re}^{Tf} - k_{pm->out}^{Tf\_apo} C_{pm}^{Tf\_apo} \tag{43}$$

$$\frac{dC_{ccp}^{Tf}}{dt} = k_{pm->ccp}^{Tf} C_{pm}^{Tf} - \left(k_{ccp->ccv_1}^{Tf} + k_{ccp->ccv_2}^{Tf}\right) C_{ccp}^{Tf} \tag{44}$$

$$\frac{dC_{ccv_1}^{Tf}}{dt} = k_{ccp->ccv_1}^{Tf} C_{ccp}^{Tf} - \left(k_{ccv_1->appl}^{Tf} + k_{ccv_1->appl^*}^{Tf}\right) C_{ccv_1}^{Tf} \tag{45}$$

$$\frac{dC_{ccv_2}^{Tf}}{dt} = k_{ccp->ccv_2}^{Tf} C_{ccp}^{Tf} - k_{ccv_2->eea1}^{Tf} C_{ccv_2}^{Tf} \tag{46}$$

$$\frac{dC_{civ}^{Tf}}{dt} = k_{pm->civ}^{Tf} C_{pm}^{Tf} - k_{civ->eea1}^{Tf} C_{civ}^{Tf} \tag{47}$$

$$\frac{dC_{appl}^{Tf}}{dt} = k_{ccv_1->appl}^{Tf} C_{ccv_1}^{Tf} - \left(k_{appl->e+a} + k_{appl->pi3p}\right) C_{appl}^{Tf} \tag{48}$$

$$\frac{dC_{e+a}^{Tf}}{dt} = k_{appl->e+a} C_{appl}^{Tf} - k_{e+a->eea1} C_{e+a}^{Tf} \tag{49}$$

$$\frac{dC_{pi3p}^{Tf}}{dt} = k_{appl->pi3p} C_{appl}^{Tf} - \left(k_{pi3p->eea1} + k_{pi3p->fre}^{Tf}\right) C_{pi3p}^{Tf} \tag{50}$$

$$\frac{dC_{appl^*}^{Tf}}{dt} = k_{ccv_1->appl^*}^{Tf} C_{ccv_1}^{Tf} + k_{e+a^*->appl^*}^{Tf} C_{e+a^*}^{Tf} - k_{appl^*->e+a^*}^{Tf} C_{appl^*}^{Tf} \tag{51}$$

$$\frac{dC_{e+a^*}^{Tf}}{dt} = k_{appl^*->e+a^*}^{Tf} C_{appl^*}^{Tf} + k_{eea1->e+a^*}^{Tf} C_{eea1}^{Tf} - \left(k_{e+a^*->eea1} + k_{e+a^*->appl^*}\right) C_{e+a^*}^{Tf} \tag{52}$$

$$\frac{dC_{eea1}^{Tf}}{dt} = k_{civ->eea1}^{Tf} C_{civ}^{Tf} + k_{ccv_2->eea1}^{Tf} C_{ccv_2}^{Tf} + k_{e+a->eea1} C_{e+a}^{Tf} + k_{e+a^*->eea1} C_{e+a^*}^{Tf} + k_{pi3p->eea1} C_{pi3p}^{Tf} - \left(\begin{matrix} k_{eea1->re}^{Tf} + k_{eea1->le}^{Tf} + \\ k_{eea1->e+a^*}^{Tf} \end{matrix}\right) C_{eea1}^{Tf} \tag{53}$$

$$\frac{dC_{le}^{Tf}}{dt} = k_{eea1->le}^{Tf} C_{eea1}^{Tf} - k_{deg} C_{le}^{Tf} \tag{54}$$

$$\frac{dC_{re}^{Tf}}{dt} = k_{eea1->re}^{Tf} C_{eea1}^{Tf} - k_{re->pm}^{Tf} C_{re}^{Tf} \tag{55}$$

$$\frac{dC_{fre}^{Tf}}{dt} = k_{pi3p->fre}^{Tf} C_{pi3p}^{Tf} - k_{fre->pm}^{Tf} C_{fre}^{Tf} \tag{56}$$

$$\frac{dC_{deg}^{Tf}}{dt} = k_{deg}^{Tf} C_{le}^{Tf} \tag{57}$$

$$\frac{dC_{out}^{Tf}}{dt} = k_{pm->out}^{Tf} C_{pm}^{Tf} + k_{pm->out}^{Tf\_apo} C_{pm}^{Tf\_apo} \tag{58}$$

The naming in model 1B is the same as in model 1A. There are two additional subscripts, appl* and e+a*, which denote stable APPL1 endosomes and their intermediate on the exchange with EEA1 endosomes.

In brief, Eqs. 27, 28, 42, 43, and 44 describe cargo balance at the plasma membrane. Eqs. 29, 30, 45, and 46 describe cargo internalization by CDE. Eqs. 31 and 47 describe internalization of cargo by CIE. Eqs. 32, 33, 34, 48, 49, and 50 describe cargo flux through APPL1-positive intermediates similar to model 1A: delivery of cargo by CCV and exit either by direct and indirect conversion and transport either through APPL1+EEA1 sort-living intermediate or PI(3)-positive EEA1-negative endosomes. The main difference of model 1B with model 1A is presented by Eqs. 35 and 36 and Eqs. 51 and 52. Eqs. 35 and 51 describe the cargo balance on a stable APPL1 compartment. Eqs. 36 and 52 describe the bi-directional cargo exchange through a stable double APPL1+EEA1 compartment between APPL1 and EEA1 endosomes. Eqs. 37 and 53 describe cargo sorting in EEA1-positive endosomes. Eqs. 38 and 54 describe cargo delivery from EEA1 endosomes to late endosomes and its consequent degradation. Eqs. 39 and 55 describe cargo flux through recycling endosomes/vesicles and its delivery to the plasma membrane. The fast recycling is described by Eq. 56. Eqs. 40 and 57 are used to calculate integral of degraded cargo. Eqs. 41 and 58 calculated integral of cargo that was released to medium.

Model 2: APPL-positive endosomes as an independent endosomal compartment. Because model 1B was not able to describe the experimental data with desired accuracy, we defined a minimal model, which would fit the experimental data of all four conditions (control and knockdown of CHC, APPL1, and EEA1) with statistically insignificant deviations ($P > 0.05$). In line with live cell imaging evidence, we assumed that APPL1+EEA1 endosomes constitute a stable compartment,

which serves as an exchange platform between APPL1 and EEA1 and can sort cargo. Because live cell imaging data provided evidence of direct (APPL1-independent) cargo delivery to APPL1+EEA1 endosomes, we added these steps in our model. However, we failed to find a model that could fit the experimental data with the required accuracy without splitting EEA1 and APPL1+EEA1 endosomes on two subpopulations, which were distinct by cargo delivery mode (CDE or CIE). After such splitting, we introduced all feasible steps of cargo transport between compartments. The model was described by 33 ODEs with 68 independent kinetic rates (supplemental models zip file: Model2). This complicated model described the experimental data with the desired accuracy. The fitting of the model set 22 parameters to zero. Surprisingly, among the eliminated steps (e.g., rates of Tf degradation, fast recycling of EGF, and other rates that were expected to be removed), we found the rates for direct exchange of cargo between two subpopulations of EEA1 and APPL1+EEA1. Then we tried to further simplify the model. To this end we set each of the remaining parameters to zero one-by-one. Those parameters, which could be set to zero in all four experimental conditions without violating the constrain p-value > 0.05, were removed. This resulted in the model of 27 ODEs with 38 independent parameters (supplemental models zip file: Model2-fix):

$$\frac{dC_{pm}^{EGF}}{dt} = \Phi_{medium}^{EGF}(t) - \left(k_{pm->cpp}^{EGF} + k_{pm->civ}^{EGF}\right)C_{pm}^{EGF} + k_{ccp->pm}^{EGF}C_{ccp}^{EGF} + k_{fre->pm}^{EGF}C_{fre}^{EGF} \quad (59)$$

$$\frac{dC_{ccp}^{EGF}}{dt} = k_{pm->ccp}^{EGF}C_{pm}^{EGF} - \left(k_{ccp->ccv_1}^{EGF} + k_{ccp->ccv_2}^{EGF} + k_{ccp->pm}^{EGF}\right)C_{ccp}^{EGF} \quad (60)$$

$$\frac{dC_{ccv_1}^{EGF}}{dt} = k_{ccp->ccv_1}^{EGF}C_{cpp}^{EGF} - k_{ccv_1->appl}^{EGF}C_{ccv_1}^{EGF} \quad (61)$$

$$\frac{dC_{ccv_2}^{EGF}}{dt} = k_{ccp->ccv_2}^{EGF}C_{cpp}^{EGF} - k_{ccv_2->eea1}^{EGF}C_{ccv_2}^{EGF} \quad (62)$$

$$\frac{dC_{civ}^{EGF}}{dt} = k_{pm->civ}^{EGF}C_{ccp}^{EGF} - \left(k_{civ->e+a^{civ}}^{EGF} + k_{civ->eea1^{civ}}^{EGF}\right)C_{civ}^{EGF} \quad (63)$$

$$\frac{dC_{appl}^{EGF}}{dt} = k_{ccv_1->appl}^{EGF}C_{ccv_1}^{EGF} - k_{appl->e+a}^{EGF}C_{appl}^{EGF} \quad (64)$$

$$\frac{dC_{e+a^{ccv}}^{EGF}}{dt} = k_{appl->e+a^{ccv}}^{EGF}C_{appl}^{EGF} - k_{e+a^{ccv}->eea1^{ccv}}^{EGF}C_{e+a^{ccv}}^{EGF} \quad (65)$$

$$\frac{dC_{e+a^{civ}}^{EGF}}{dt} = k_{civ->e+a}^{EGF}C_{civ}^{EGF} + k_{eea1^{civ}->e+a^{civ}}^{EGF}C_{eea1^{civ}}^{EGF} - k_{e+a^{civ}->eea1^{civ}}^{EGF}C_{e+a^{civ}}^{EGF} \quad (66)$$

$$\frac{dC_{eea1^{ccv}}^{EGF}}{dt} = k_{ccv_2->eea1}^{EGF}C_{ccv_2}^{EGF} + k_{e+a^{ccv}->eea1^{ccv}}^{EGF}C_{e+a^{ccv}}^{EGF} - \left(k_{eea1^{ccv}->e+a^{ccv}}^{EGF} + k_{eea1->re}^{EGF}\right)C_{eea1^{ccv}}^{EGF} \quad (67)$$

$$\frac{dC_{eea1^{civ}}^{EGF}}{dt} = k_{civ->eea1}^{EGF}C_{civ}^{EGF} + k_{e+a^{civ}->eea1^{civ}}^{EGF}C_{e+a^{civ}}^{EGF} - \left(k_{eea1^{civ}->e+a^{civ}}^{EGF} + k_{eea1->le}^{EGF}\right)C_{eea1^{civ}}^{EGF} \quad (68)$$

$$\frac{dC_{le}^{EGF}}{dt} = k_{eea1->le}^{EGF}C_{eea1^{civ}}^{EGF} - k_{deg}C_{le}^{EGF} \quad (69)$$

$$\frac{dC_{re}^{EGF}}{dt} = k_{eea1->re}^{EGF}C_{eea1^{re}}^{EGF} - k_{re->pm}^{EGF}C_{re}^{EGF} \quad (70)$$

$$\frac{dC_{deg}^{EGF}}{dt} = k_{deg}^{EGF}C_{le}^{EGF} \quad (71)$$

$$\frac{dC_{pm}^{Tf}}{dt} = \Phi_{medium}^{Tf}(t) + k_{ccp->pm}^{Tf}C_{ccp}^{Tf} - \left(k_{pm->ccp}^{Tf} + k_{pm->civ}^{Tf}\right)C_{pm}^{Tf} \quad (72)$$

$$\frac{dC_{pm}^{Tf\_apo}}{dt} = k_{fre->pm}^{Tf}C_{fre}^{Tf} + k_{re->pm}^{Tf}C_{re}^{Tf} - k_{pm->out}^{Tf\_apo}C_{pm}^{Tf\_apo} \quad (73)$$

$$\frac{dC_{ccp}^{Tf}}{dt} = k_{pm->ccp}^{Tf}C_{pm}^{Tf} - \left(k_{ccp->ccv1}^{Tf} + k_{ccp->ccv1}^{Tf}\right)C_{ccp}^{Tf} \quad (74)$$

$$\frac{dC_{ccv_1}^{Tf}}{dt} = k_{ccp->ccv1}^{Tf}C_{ccp}^{Tf} - \left(k_{ccv_1->appl}^{Tf} + k_{ccv_1->e+a^{civ}}^{Tf}\right)C_{ccv_1}^{Tf} \quad (75)$$

$$\frac{dC_{ccv_2}^{Tf}}{dt} = k_{ccp->ccv_2}^{Tf}C_{ccp}^{Tf} - k_{ccv_2->eea1}^{Tf}C_{ccv_2}^{Tf} \quad (76)$$

$$\frac{dC_{civ}^{Tf}}{dt} = k_{pm->civ}^{Tf}C_{pm}^{Tf} - \left(k_{civ->eea1}^{Tf} + k_{civ->e+a^{civ}}^{Tf}\right)C_{civ}^{Tf} \quad (77)$$

$$\frac{dC_{appl}^{Tf}}{dt} = k_{ccv_1->appl}^{Tf}C_{ccv_1}^{Tf} + k_{e+a^{ccv}->appl}^{Tf}C_{e+a^{ccv}}^{Tf} - \left(k_{appl->fre}^{Tf} + k_{appl->a+e^{civ}}^{Tf}\right)C_{appl}^{Tf} \quad (78)$$

$$\frac{dC_{e+a^{ccv}}^{Tf}}{dt} = k_{ccv_1->e+a^{ccv}}^{Tf}C_{ccv_1}^{Tf} + k_{eea1^{ccv}->e+a^{ccv}}^{Tf}C_{eea1^{ccv}}^{Tf} - k_{e+a^{ccv}->appl}^{Tf}C_{e+a^{ccv}}^{Tf} \quad (79)$$

$$\frac{dC_{e+a^{civ}}^{Tf}}{dt} = k_{civ->e+a^{civ}}^{Tf}C_{civ}^{Tf} + k_{appl->e+a^{civ}}^{Tf}C_{eea1}^{Tf} - \left(k_{e+a^{civ}->re}^{Tf} + k_{e+a^{civ}->eea1^{civ}}^{Tf}\right)C_{e+a^{civ}}^{Tf} \quad (80)$$

$$\frac{dC_{eea1^{ccv}}^{Tf}}{dt} = k_{ccv_2->eea1}^{Tf}C_{ccv_2}^{Tf} - k_{eea1^{ccv}->e+a^{ccv}}^{Tf}C_{eea1^{ccv}}^{Tf} \quad (81)$$

$$\frac{dC_{eea1^{civ}}^{Tf}}{dt} = k_{civ->eea1}^{Tf}C_{civ}^{Tf} + k_{e+a^{civ}->eea1^{civ}}^{Tf}C_{e+a^{civ}}^{Tf} - k_{eea1^{civ}->re}^{Tf}C_{eea1^{civ}}^{Tf} \quad (82)$$

$$\frac{dC_{re}^{Tf}}{dt} = k_{eea1^{civ}->re}^{Tf}C_{eea1^{civ}}^{Tf} + k_{e+a^{civ}->re}^{Tf}C_{e+a^{civ}}^{Tf} - k_{re->pm}^{Tf}C_{re}^{Tf} \quad (83)$$

$$\frac{dC_{fre}^{Tf}}{dt} = k_{appl->fre}^{Tf}C_{appl}^{Tf} - k_{fre->pm}^{Tf}C_{fre}^{Tf} \quad (84)$$

$$\frac{dC_{out}^{Tf}}{dt} = k_{pm->out}^{Tf\_apo}C_{pm}^{Tf\_apo} \quad (85)$$

The naming in the model 2 is similar to that in models 1A and 1B. Two subpopulations of EEA1 and APPL1+EEA1 endosomes are marked according to the main route of cargo delivery by superscripts CCV and CIV. For example: $C_{EEA1^{ccv}}^{EGF}$ means the amount of EGF in the EEA1 sub-population that gets the cargo mostly by CDE, $C_{e+a^{civ}}^{Tf}$ means the amount of Tf in the APPL1+EEA1 subpopulation that gets the cargo mostly by CIE.

In model 2, Eqs. 59, 60, 72, 73, and 74 describe cargo binding/unbinding to/from receptors on PM and either incorporation to CCP followed by internalization by CCV or internalization by CIE. Eqs. 61, 62, 63, 75, 76, and 77 describe cargo internalization by clathrin-covered and clathrin-independent vesicles. As we did in model 1A and

1B, we denote CCVs that deliver cargo to APPL1 as CCV_1 and those that deliver cargo to EEA1 as CCV_2. Eqs. 64 and 78 describe cargo balance in APPL1-positive compartment: delivery of cargo by CCV sorting, transport to APPL1+EEA1 endosomes, and back-flux of Tf from APPL1+EEA1 compartment. Eqs. 65, 66, 79, and 80 describe cargo processing (receiving, sorting, and transmitting) by two subpopulations of APPL1+EEA1 endosomes. Eqs. 67, 68, 81, and 82 describe cargo sorting in EEA1-positive endosomes. Eq. 69 describes cargo traffic from EEA1 endosomes to late endosomes and degradation. Eqs. 70 and 83 describe cargo recycling by slow recycling routes. The fast recycling is described by Eq. 84. Eqs. 71 and 85 are used to calculate integral of cargo that was degraded or released to medium.

Fitting models to experimental data

Because the experiments were done in four replicas performed sequentially with variable time intervals between them, one could not assume that the intensities of the microscope lasers were stable over time. Therefore, we used colocalizations (ratio of integral intensity of colocalized marker to the total integral intensity) of respective cargo with APPL1, EEA1, or APPL1+EEA1 or to none of them, which are relative and do not depend on the fluctuation of the microscope laser power. In addition we used (a) the integral vesicular intensity of cargo and (b) integral nonvesicular intensity. The integral nonvesicular intensity was corrected for background intensities outside of cells and as such was proportional to the membrane-bound cargo. Because in our analysis we used only one confocal section of cells (close to the coverslip), the amount of detected PM-bound cargo could be as overrepresented as underrepresented, depending on the receptor spatial localization on PM. We did not make any a priori assumption about receptor localization. Instead, we introduced free scale parameter for nonvesicular intensity, which was fitted with parameters of the model.

The fit of EEA1 knockdown was different from other conditions. In contrast with APPL1 down-regulation, where the amount of residual APPL1 (30%) was enough to reliably detect APPL1 and APPL1+EEA1 endosomes (Fig. S4, A and B), the down-regulation of EEA1 was much stronger (residual EEA1 ~10%). This could result in the misclassification of part of APPL1+EEA1 endosomes as APPL1 endosomes because the EEA1 signal could be below the detection limit. To account for this effect, we introduced additional parameter(s):

$$mdl\_C_{appl}^{EGF} = C_{appl}^{EGF} + (1 - \varepsilon) \cdot C_{e+a}^{EGF}$$

$$mdl\_C_{appl}^{Tf} = C_{appl}^{Tf} + (1 - \varepsilon) \cdot C_{e+a}^{Tf}$$

$$mdl\_C_{e+a}^{EGF} = \varepsilon \cdot C_{e+a}^{EGF}$$

$$mdl\_C_{e+a}^{Tf} = \varepsilon \cdot C_{e+a}^{Tf},$$

where mdl_C denotes the model curve to compare with experiment.

In case of multiple types of APPL1+EEA1 endosomes (e.g., in model 1B and model 2) the parameters (ε_1, ε_2) were fitted independently.

In the models, the amount of cargo in the medium was set to 1 in arbitrary units (cargo pulse was modeled by unit pulse function). As a result, the model predicts the kinetics of cargo transport in arbitrary units. In the experiments, we measured the integral intensity of fluorescence, which is proportional to the amount of cargo, but the coefficient of proportionality is unknown. To compare the theory pre-

dictions with the experimental data, we introduced a scale factor, which is equal to the ratio between the integral intensity of fluorescence to the unit of cargo amount in the model. Because this factor is not known in advance, it has to be found during the model fitting procedure. To decrease the number of parameters to fit, the scaling factor for vesicular intensity $s_{vesicular}$ was found independently for each iteration of the fitting procedure by a maximum likelihood formula:

$$s_{vesicular} = \frac{\sum_{i=1}^{14} \frac{y_i x_i}{\sigma_i^2}}{\sum_{i=1}^{14} \frac{x_i^2}{\sigma_i^2}},$$

where x_i is the theoretical prediction for time point i, y_i is the experimental value for time point i, and σ_i is the SEM of the experimental value for time point i.

The analysis of total (vesicular and nonvesicular) intensity is more complex. The total fluorescence intensity of the cell includes the fluorescence of the plasma membrane-bound cargo, the one of the endocytosed cargo as well as unknown background (offset) from autofluorescence and noise of the microscope, i.e., it includes the scaling factor and offset. Similar to vesicular intensity, a maximum likelihood procedure was used to find the scale factor s_{total} and offset for total cargo intensity f_{total}:

$$s_{total} = \frac{\sum_{i=1}^{14} \frac{y_i x_i}{\sigma_i^2} \cdot \sum_{i=1}^{14} \frac{1}{\sigma_i^2} - \sum_{i=1}^{14} \frac{y_i}{\sigma_i^2} \cdot \sum_{i=1}^{14} \frac{x_i}{\sigma_i^2}}{\sum_{i=1}^{14} \frac{x_i^2}{\sigma_i^2} \cdot \sum_{i=1}^{14} \frac{1}{\sigma_i^2} - \left(\sum_{i=1}^{14} \frac{x_i}{\sigma_i^2}\right)^2}$$

and

$$f_{total} = \frac{\sum_{i=1}^{14} \frac{x_i y_i}{\sigma_i^2} - s_{total} \sum_{i=1}^{14} \frac{x_i^2}{\sigma_i^2}}{\sum_{i=1}^{14} \frac{x_i}{\sigma_i^2}}$$

In contrast, the colocalization ratio (the ratio of the amount of cargo on a specific compartment to the total amount of cargo in the cell) cancels the scaling factor and, as such, the experimental data can be directly compared with the theory prediction.

To compensate for the apparent colocalization by occlusion or diffraction blurring, we calculated the "random colocalization" by randomly shuffling cargo vesicles. The shift was performed independently for every endosome on a random distance that was limited to 8 times the size of a respective endosome. This shift was large enough to eliminate the real colocalization but small enough to preserve the local density of vesicles and, thus, preserve the random colocalization. After random shuffling the colocalization was calculated and used as an estimation of random colocalization. The corrected colocalization was calculated as descibed in Kalaidzidis et al. (2015).

Altogether, we used 12 experimental kinetics to compare with the model: (a) total nonvesicular cargo intensity, (b) total vesicular cargo intensity, (c) colocalization with EEA1, (d) colocalization with APPL1 and (e) colocalization with EEA1+APPL1, (f) proportion of vesicular cargo that did not colocalize with any of APPL1 or EEA1 for both types of cargo. Because every kinetic has 14 time points, we compared 168 experimental values with the theoretical predictions. Because the number of experimental points is higher than the number of model parameters, we extracted the parameters by multidimensional fitting.

The fitting was performed by the FitModel64 software package (Zeigerer et al., 2012). The fitting procedure used a custom deterministic optimization procedure, which interchangeably use Davidon-Fletcher-Powell quasi-Newton multidimensional optimization with direction-set (Powell) method (Press et al., 1992). This

deterministic optimization method was incorporated in the nondeterministic quasi-annealing algorithm (Griffiths et al., 1999. In short, the algorithm runs a set of parallel searching threads. Each one chooses a random starting point by "temperature"-dependent variation of the best found solution and performs a deterministic search for a minimum. This procedure iterates a predefined number of cycles. In each iteration, the "temperature" gradually decreases. At the end of the procedure the best found solution is taken. In our study, we used 300 threads with 5 iterations. The files with the models are provided in the supplemental models zip file.

We ruled out that traffic alteration after APPL1 and EEA1 knockdowns are consequence of altered receptor levels on the plasma membrane. We measured the total amount of Tf and EGF bound to the cell at the end of the 30-s pulse and found that the binding of ligand on the cell surface was not significantly perturbed (Fig.S4 C).

Parameters of models 1A, 1B, and 2
The parameters of models are provided in the supplemental models zip file.

Online supplemental material
Online supplemental materials include control microscopy images and quantification of validation of fluorescently tagged constructs of APPL1 and EEA1; controls for CHC, APPL1, and EEA1 knockdowns; and detailed fit of models 1A, 1B, and 2 to the experimental data. Videos 1–9 illustrate the panels presented in Figs. 4 and 5. Fig. S1 shows (a) localization of APPL1 with respect to various compartment markers (Sec61, GM130, γ-adaptin, LAMP1, Rab7, GPI, myo6, and EEA1) in HeLa cells; (b) quantification of EGF and Tf pulse-chase3 kinetics; and (c) number and mean integral intensities of APPL1 and EEA1 endosomes during pulse-chase experiment. Fig. S2 shows validation of N-terminal EGFP-tagged construct of APPL1. Fig. S3 shows comparison of experimental data with predictions from models 1A and 1B. Fig. S4 shows quantification of endocytic system alteration by down-regulation of CHC, APPL1, and EEA1. Fig. S5 shows comparison of experimental data with model 2 predictions. Online supplemental material is available at http://www.jcb.org/cgi/content/full/jcb.201511117DC1.

References

Bökel, C., A. Schwabedissen, E. Entchev, O. Renaud, and M. González-Gaitán. 2006. Sara endosomes and the maintenance of Dpp signaling levels across mitosis. *Science.* 314:1135–1139. http://dx.doi.org/10.1126/science.1132524

Chavrier, P., R.G. Parton, H.P. Hauri, K. Simons, and M. Zerial. 1990. Localization of low molecular weight GTP binding proteins to exocytic and endocytic compartments. *Cell.* 62:317–329. http://dx.doi.org/10.1016/0092-8674(90)90369-P

Chen, H., and P. De Camilli. 2005. The association of epsin with ubiquitinated cargo along the endocytic pathway is negatively regulated by its interaction with clathrin. *Proc. Natl. Acad. Sci. USA.* 102:2766–2771. http://dx.doi.org/10.1073/pnas.0409719102

Cheng, K.K., K.S. Lam, D. Wu, Y. Wang, G. Sweeney, R.L. Hoo, J. Zhang, and A. Xu. 2012. APPL1 potentiates insulin secretion in pancreatic β cells by enhancing protein kinase Akt-dependent expression of SNARE proteins in mice. *Proc. Natl. Acad. Sci. USA.* 109:8919–8924. http://dx.doi.org/10.1073/pnas.120243510922566644

Cheng, Y., W. Boll, T. Kirchhausen, S.C. Harrison, and T. Walz. 2007. Cryo-electron tomography of clathrin-coated vesicles: structural implications for coat assembly. *J. Mol. Biol.* 365:892–899. http://dx.doi.org/10.1016/j.jmb.2006.10.036

Christoforidis, S., H.M. McBride, R.D. Burgoyne, M. Zerial. 1999. The Rab5 effector EEA1 is a core component of endosome docking. *Nature.* 397:621–625. http://dx.doi.org/10.1038/17618

Collinet, C., M. Stöter, C.R. Bradshaw, N. Samusik, J.C. Rink, D. Kenski, B. Habermann, F. Buchholz, R. Henschel, M.S. Mueller, et al. 2010. Systems survey of endocytosis by multiparametric image analysis. *Nature.* 464:243–249. http://dx.doi.org/10.1038/nature08779

Conner, S.D., and S.L. Schmid. 2003. Regulated portals of entry into the cell. *Nature.* 422:37–44. http://dx.doi.org/10.1038/nature01451

Danson, C., E. Brown, O.J. Hemmings, I.J. McGough, S. Yarwood, K.J. Heesom, J.G. Carlton, J. Martin-Serrano, M.T. May, P. Verkade, and P.J. Cullen. 2013. SNX15 links clathrin endocytosis to the PtdIns3P early endosome independently of the APPL1 endosome. *J. Cell Sci.* 126:4885–4899. http://dx.doi.org/10.1242/jcs.125732

Dautry-Varsat, A., A. Ciechanover, and H.F. Lodish. 1983. pH and the recycling of transferrin during receptor-mediated endocytosis. *Proc. Natl. Acad. Sci. USA.* 80:2258–2262. http://dx.doi.org/10.1073/pnas.80.8.2258

Deepa, S.S., and L.Q. Dong. 2009. APPL1: role in adiponectin signaling and beyond. *Am. J. Physiol. Endocrinol. Metab.* 296:E22–E36. http://dx.doi.org/10.1152/ajpendo.90731.2008

Di Fiore, P.P., and M. von Zastrow. 2014. Endocytosis, signaling, and beyond. *Cold Spring Harb. Perspect. Biol.* 6:a016865. http://dx.doi.org/10.1101/cshperspect.a016865

Doherty, G.J., and H.T. McMahon. 2009. Mechanisms of endocytosis. *Annu. Rev. Biochem.* 78:857–902. http://dx.doi.org/10.1146/annurev.biochem.78.081307.110540

Ehrlich, M., W. Boll, A. Van Oijen, R. Hariharan, K. Chandran, M.L. Nibert, and T. Kirchhausen. 2004. Endocytosis by random initiation and stabilization of clathrin-coated pits. *Cell.* 118:591–605. http://dx.doi.org/10.1016/j.cell.2004.08.017

Erdmann, K.S., Y. Mao, H.J. McCrea, R. Zoncu, S. Lee, S. Paradise, J. Modregger, D. Biemesderfer, D. Toomre, and P. De Camilli. 2007. A role of the Lowe syndrome protein OCRL in early steps of the endocytic pathway. *Dev. Cell.* 13:377–390. http://dx.doi.org/10.1016/j.devcel.2007.08.004

Flores-Rodriguez, N., D.A. Kenwright, P.H. Chung, A.W. Harrison, F. Stefani, T.A. Waigh, V.J. Allan, and P.G. Woodman. 2015. ESCRT-0 marks an APPL1-independent transit route for EGFR between the cell surface and the EEA1-positive early endosome. *J. Cell Sci.* 128:755–767. http://dx.doi.org/10.1242/jcs.161786

Foret, L., J.E. Dawson, R. Villaseñor, C. Collinet, A. Deutsch, L. Brusch, M. Zerial, Y. Kalaidzidis, and F. Jülicher. 2012. A general theoretical

framework to infer endosomal network dynamics from quantitative image analysis. *Curr. Biol.* 22:1381–1390. http://dx.doi.org/10.1016/j.cub.2012.06.021

Gallop, J.L., and H.T. McMahon. 2005. BAR domains and membrane curvature: bringing your curves to the BAR. *Biochem. Soc. Symp.* 72:223–231. http://dx.doi.org/10.1042/bss0720223

Gan, Z., S. Ram, R.J. Ober, and E.S. Ward. 2013. Using multifocal plane microscopy to reveal novel trafficking processes in the recycling pathway. *J. Cell Sci.* 126:1176–1188. http://dx.doi.org/10.1242/jcs.116327

Griffiths, T.R., D.A. Nerukh, and S.A. Eremenko. 1999. The application of theoretical models of complex shape to the fitting of experimental spectra having closely overlapping bands. *Phys. Chem. Chem. Phys.* 1:3199–3208. http://dx.doi.org/10.1039/a902569c

Hayakawa, A., D. Leonard, S. Murphy, S. Hayes, M. Soto, K. Fogarty, C. Standley, K. Bellve, D. Lambright, C. Mello, and S. Corvera. 2006. The WD40 and FYVE domain containing protein 2 defines a class of early endosomes necessary for endocytosis. *Proc. Natl. Acad. Sci. USA.* 103:11928–11933. http://dx.doi.org/10.1073/pnas.0508832103

Henschel, A., F. Buchholz, and B. Habermann. 2004. DEQOR: a web-based tool for the design and quality control of siRNAs. *Nucleic Acids Res.* 32(Web Server):W113-20. http://dx.doi.org/10.1093/nar/gkh408

Horiuchi, H., R. Lippé, H.M. McBride, M. Rubino, P. Woodman, H. Stenmark, V. Rybin, M. Wilm, K. Ashman, M. Mann, and M. Zerial. 1997. A novel Rab5 GDP/GTP exchange factor complexed to Rabaptin-5 links nucleotide exchange to effector recruitment and function. *Cell.* 90:1149–1159. http://dx.doi.org/10.1016/S0092-8674(00)80380-3

Howes, M.T., M. Kirkham, J. Riches, K. Cortese, P.J. Walser, F. Simpson, M.M. Hill, A. Jones, R. Lundmark, M.R. Lindsay, et al. 2010. Clathrin-independent carriers form a high capacity endocytic sorting system at the leading edge of migrating cells. *J. Cell Biol.* 190:675–691. http://dx.doi.org/10.1083/jcb.201002119

Hupalowska, A., B. Pyrzynska, and M. Miaczynska. 2012. APPL1 regulates basal NF-κB activity by stabilizing NIK. *J. Cell Sci.* 125:4090–4102. http://dx.doi.org/10.1242/jcs.105171

Kalaidzidis, Ya., I. Kalaidzidis, and M. Zerial. 2015. A probabilistic method to quantify the colocalization of markers on intracellular vesicular structures visualized by light microscopy. *AIP Conf. Proc.* 1:580–587.

Kittler, R., A.K. Heninger, K. Franke, B. Habermann, and F. Buchholz. 2005. Production of endoribonuclease-prepared short interfering RNAs for gene silencing in mammalian cells. *Nat. Methods.* 2:779–784. http://dx.doi.org/10.1038/nmeth1005-779

Kural, C., S.K. Tacheva-Grigorova, S. Boulant, E. Cocucci, T. Baust, D. Duarte, and T. Kirchhausen. 2012. Dynamics of intracellular clathrin/AP1- and clathrin/AP3-containing carriers. *Cell Reports.* 2:1111–1119. http://dx.doi.org/10.1016/j.celrep.2012.09.025

Lakadamyali, M., M.J. Rust, and X. Zhuang. 2006. Ligands for clathrin-mediated endocytosis are differentially sorted into distinct populations of early endosomes. *Cell.* 124:997–1009. http://dx.doi.org/10.1016/j.cell.2005.12.038

Leonard, D., A. Hayakawa, D. Lawe, D. Lambright, K.D. Bellve, C. Standley, L.M. Lifshitz, K.E. Fogarty, and S. Corvera. 2008. Sorting of EGF and transferrin at the plasma membrane and by cargo-specific signaling to EEA1-enriched endosomes. *J. Cell Sci.* 121:3445–3458. http://dx.doi.org/10.1242/jcs.031484

Lim, J.P., and P.A. Gleeson. 2011. Macropinocytosis: an endocytic pathway for internalising large gulps. *Immunol. Cell Biol.* 89:836–843. http://dx.doi.org/10.1038/icb.2011.20

Lin, D.C., C. Quevedo, N.E. Brewer, A. Bell, J.R. Testa, M.L. Grimes, F.D. Miller, and D.R. Kaplan. 2006. APPL1 associates with TrkA and GIPC1 and is required for nerve growth factor-mediated signal transduction. *Mol. Cell. Biol.* 26:8928–8941. http://dx.doi.org/10.1128/MCB.00228-06

Macia, E., M. Ehrlich, R. Massol, E. Boucrot, C. Brunner, and T. Kirchhausen. 2006. Dynasore, a cell-permeable inhibitor of dynamin. *Dev. Cell.* 10:839–850. http://dx.doi.org/10.1016/j.devcel.2006.04.002

Majumdar, D., C.A. Nebhan, L. Hu, B. Anderson, and D.J. Webb. 2011. An APPL1/Akt signaling complex regulates dendritic spine and synapse formation in hippocampal neurons. *Mol. Cell. Neurosci.* 46:633–644. http://dx.doi.org/10.1016/j.mcn.2011.01.003

Mao, X., C.K. Kikani, R.A. Riojas, P. Langlais, L. Wang, F.J. Ramos, Q. Fang, C.Y. Christ-Roberts, J.Y. Hong, R.Y. Kim, et al. 2006. APPL1 binds to adiponectin receptors and mediates adiponectin signalling and function. *Nat. Cell Biol.* 8:516–523. http://dx.doi.org/10.1038/ncb1404

Mayor, S., and R.E. Pagano. 2007. Pathways of clathrin-independent endocytosis. *Nat. Rev. Mol. Cell Biol.* 8:603–612. http://dx.doi.org/10.1038/nrm2216

Miaczynska, M., S. Christoforidis, A. Giner, A. Shevchenko, S. Uttenweiler-Joseph, B. Habermann, M. Wilm, R.G. Parton, and M. Zerial. 2004. APPL proteins link Rab5 to nuclear signal transduction via an endosomal compartment. *Cell.* 116:445–456. http://dx.doi.org/10.1016/S0092-8674(04)00117-5

Mitsuuchi, Y., S.W. Johnson, G. Sonoda, S. Tanno, E.A. Golemis, and J.R. Testa. 1999. Identification of a chromosome 3p14.3-21.1 gene, APPL, encoding an adaptor molecule that interacts with the oncoprotein-serine/threonine kinase AKT2. *Oncogene.* 18:4891–4898. http://dx.doi.org/10.1038/sj.onc.1203080

Motley, A., N.A. Bright, M.N. Seaman, and M.S. Robinson. 2003. Clathrin-mediated endocytosis in AP-2-depleted cells. *J. Cell Biol.* 162:909–918. http://dx.doi.org/10.1083/jcb.200305145

Navaroli, D.M., K.D. Bellvé, C. Standley, L.M. Lifshitz, J. Cardia, D. Lambright, D. Leonard, K.E. Fogarty, and S. Corvera. 2012. Rabenosyn-5 defines the fate of the transferrin receptor following clathrin-mediated endocytosis. *Proc. Natl. Acad. Sci. USA.* 109:E471–E480. http://dx.doi.org/10.1073/pnas.1115495109

Ohya, T., M. Miaczynska, U. Coskun, B. Lommer, A. Runge, D. Drechsel, Y. Kalaidzidis, and M. Zerial. 2009. Reconstitution of Rab- and SNARE-dependent membrane fusion by synthetic endosomes. *Nature.* 459:1091–1097. http://dx.doi.org/10.1038/nature08107

Perini, E.D., R. Schaefer, M. Stöter, Y. Kalaidzidis, and M. Zerial. 2014. Mammalian CORVET is required for fusion and conversion of distinct early endosome subpopulations. *Traffic.* 15:1366–1389. http://dx.doi.org/10.1111/tra.12232

Perret, E., A. Lakkaraju, S. Deborde, R. Schreiner, and E. Rodriguez-Boulan. 2005. Evolving endosomes: how many varieties and why? *Curr. Opin. Cell Biol.* 17:423–434. http://dx.doi.org/10.1016/j.ceb.2005.06.008

Pfeffer, S.R. 2013. Rab GTPase regulation of membrane identity. *Curr. Opin. Cell Biol.* 25:414–419. http://dx.doi.org/10.1016/j.ceb.2013.04.002

Poteryaev, D., S. Datta, K. Ackema, M. Zerial, and A. Spang. 2010. Identification of the switch in early-to-late endosome transition. *Cell.* 141:497–508. http://dx.doi.org/10.1016/j.cell.2010.03.011

Press, W.H., S.A. Teukolsky, W.T. Vetterling, and B.P. Flannery. 1992. Numerical Recipes in C. Cambridge University Press, Cambridge.

Puthenveedu, M.A., and M. von Zastrow. 2006. Cargo regulates clathrin-coated pit dynamics. *Cell.* 127:113–124. http://dx.doi.org/10.1016/j.cell.2006.08.035

Rashid, S., I. Pilecka, A. Torun, B. Olchowik, B. Bielinska, and M. Miaczynska. 2009. Endosomal adaptor proteins APPL1 and APPL2 are novel activators of beta-catenin/TCF-mediated transcription. *J. Biol. Chem.* 284:18115–18128. http://dx.doi.org/10.1074/jbc.M109.007237

Rink, J., E. Ghigo, Y. Kalaidzidis, and M. Zerial. 2005. Rab conversion as a mechanism of progression from early to late endosomes. *Cell.* 122:735–749. http://dx.doi.org/10.1016/j.cell.2005.06.043

Sadowski, L., I. Pilecka, and M. Miaczynska. 2009. Signaling from endosomes: location makes a difference. *Exp. Cell Res.* 315:1601–1609. http://dx.doi.org/10.1016/j.yexcr.2008.09.021

Saffarian, S., E. Cocucci, and T. Kirchhausen. 2009. Distinct dynamics of endocytic clathrin-coated pits and coated plaques. *PLoS Biol.* 7:e1000191. http://dx.doi.org/10.1371/journal.pbio.1000191

Schenck, A., L. Goto-Silva, C. Collinet, M. Rhinn, A. Giner, B. Habermann, M. Brand, and M. Zerial. 2008. The endosomal protein Appl1 mediates Akt substrate specificity and cell survival in vertebrate development. *Cell.* 133:486–497. http://dx.doi.org/10.1016/j.cell.2008.02.044

Sigismund, S., T. Woelk, C. Puri, E. Maspero, C. Tacchetti, P. Transidico, P.P. Di Fiore, and S. Polo. 2005. Clathrin-independent endocytosis of ubiquitinated cargos. *Proc. Natl. Acad. Sci. USA.* 102:2760–2765. http://dx.doi.org/10.1073/pnas.0409817102

Sigismund, S., E. Argenzio, D. Tosoni, E. Cavallaro, S. Polo, and P.P. Di Fiore. 2008. Clathrin-mediated internalization is essential for sustained EGFR signaling but dispensable for degradation. *Dev. Cell.* 15:209–219. http://dx.doi.org/10.1016/j.devcel.2008.06.012

Simonsen, A., R. Lippé, S. Christoforidis, J.-M. Gaullier, A. Brech, J. Callaghan, B.-H. Toh, C. Murphy, M. Zerial, and H. Stenmark. 1998. EEA1 links PI(3)K function to Rab5 regulation of endosome fusion. *Nature.* 394:494–498. http://dx.doi.org/10.1038/28879

Sivia, D.S., and C.J. Carlile. 1992. Molecular-spectroscopy and Bayesian spectral-analysis - how many lines are there. *J. Chem. Phys.* 96:170–178. http://dx.doi.org/10.1063/1.462505

Sönnichsen, B., S. De Renzis, E. Nielsen, J. Rietdorf, and M. Zerial. 2000. Distinct membrane domains on endosomes in the recycling pathway visualized by multicolor imaging of Rab4, Rab5, and Rab11. *J. Cell Biol.* 149:901–914. http://dx.doi.org/10.1083/jcb.149.4.901

Sorkin, A., and M. von Zastrow. 2009. Endocytosis and signalling: intertwining molecular networks. *Nat. Rev. Mol. Cell Biol.* 10:609–622. http://dx.doi.org/10.1038/nrm2748

Stang, E., F.D. Blystad, M. Kazazic, V. Bertelsen, T. Brodahl, C. Raiborg, H. Stenmark, and I.H. Madshus. 2004. Cbl-dependent ubiquitination is required for progression of EGF receptors into clathrin-coated pits. *Mol. Biol. Cell.* 15:3591–3604. http://dx.doi.org/10.1091/mbc.E04-01-0041

Stenmark, H. 2009. Rab GTPases as coordinators of vesicle traffic. *Nat. Rev. Mol. Cell Biol.* 10:513–525. http://dx.doi.org/10.1038/nrm2728

Tosoni, D., C. Puri, S. Confalonieri, A.E. Salcini, P. De Camilli, C. Tacchetti, and P.P. Di Fiore. 2005. TTP specifically regulates the internalization of the transferrin receptor. *Cell.* 123:875–888. http://dx.doi.org/10.1016/j.cell.2005.10.021

Varsano, T., M.Q. Dong, I. Niesman, H. Gacula, X. Lou, T. Ma, J.R. Testa, J.R. Yates III, and M.G. Farquhar. 2006. GIPC is recruited by APPL to peripheral TrkA endosomes and regulates TrkA trafficking and signaling. *Mol. Cell. Biol.* 26:8942–8952. http://dx.doi.org/10.1128/MCB.00305-06

Varsano, T., V. Taupin, L. Guo, O.Y. Baterina Jr., and M.G. Farquhar. 2012. The PDZ protein GIPC regulates trafficking of the LPA1 receptor from APPL signaling endosomes and attenuates the cell's response to LPA. *PLoS ONE.* 7:e49227. http://dx.doi.org/10.1371/journal.pone.0049227

Wang, Y.B., J.J. Wang, S.H. Wang, S.S. Liu, J.Y. Cao, X.M. Li, S. Qiu, and J.H. Luo. 2012. Adaptor protein APPL1 couples synaptic NMDA receptor with neuronal prosurvival phosphatidylinositol 3-kinase/Akt pathway. *J. Neurosci.* 32:11919–11929. http://dx.doi.org/10.1523/JNEUROSCI.3852-11.2012

Xin, X., L. Zhou, C.M. Reyes, F. Liu, and L.Q. Dong. 2011. APPL1 mediates adiponectin-stimulated p38 MAPK activation by scaffolding the TAK1-MKK3-p38 MAPK pathway. *Am. J. Physiol. Endocrinol. Metab.* 300:E103–E110. http://dx.doi.org/10.1152/ajpendo.00427.2010

Zeigerer, A., J. Gilleron, R.L. Bogorad, G. Marsico, H. Nonaka, S. Seifert, H. Epstein-Barash, S. Kuchimanchi, C.G. Peng, V.M. Ruda, et al. 2012. Rab5 is necessary for the biogenesis of the endolysosomal system in vivo. *Nature.* 485:465–470. http://dx.doi.org/10.1038/nature11133

Zerial, M., and H. McBride. 2001. Rab proteins as membrane organizers. *Nat. Rev. Mol. Cell Biol.* 2:107–117. http://dx.doi.org/10.1038/35052055

Zoncu, R., R.M. Perera, D.M. Balkin, M. Pirruccello, D. Toomre, and P. De Camilli. 2009. A phosphoinositide switch controls the maturation and signaling properties of APPL endosomes. *Cell.* 136:1110–1121. http://dx.doi.org/10.1016/j.cell.2009.01.032